



Article

Three-D Mineralogical Mapping of the Kovdor Phoscorite–Carbonatite Complex, NW Russia: I. Forsterite

Julia A. Mikhailova ^{1,2}, Gregory Yu. Ivanyuk ^{1,2,*}, Andrey O. Kalashnikov ² ,
Yakov A. Pakhomovsky ^{1,2}, Ayya V. Bazai ^{1,2}, Taras L. Panikorovskii ¹ ,
Victor N. Yakovenchuk ^{1,2}, Nataly G. Konopleva ¹ and Pavel M. Goryainov ²

¹ Nanomaterials Research Centre of Kola Science Centre, Russian Academy of Sciences, 14 Fersman Street, Apatity 184209, Russia; ylya_korchak@mail.ru (J.A.M.); pakhom@geoksc.apatity.ru (Y.A.P.); bazai@geoksc.apatity.ru (A.V.B.); taras.panikorovsky@spbu.ru (T.L.P.); yakovenchuk@geoksc.apatity.ru (V.N.Y.); konoplyova55@mail.ru (N.G.K.)

² Geological Institute of Kola Science Centre, Russian Academy of Sciences, 14 Fersman Street, Apatity 184209, Russia; kalashnikov@geoksc.apatity.ru (A.O.K.); pgor@geoksc.apatity.ru (P.M.G.)

* Correspondence: g.ivanyuk@gmail.com; Tel.: +7-81555-79531

Received: 30 May 2018; Accepted: 16 June 2018; Published: 20 June 2018



Abstract: The Kovdor alkaline-ultrabasic massif (NW Russia) is formed by three consequent intrusions: peridotite, foidolite–melilitolite and phoscorite–carbonatite. Forsterite is the earliest mineral of both peridotite and phoscorite–carbonatite, and its crystallization governed evolution of magmatic systems. Crystallization of forsterite from Ca-Fe-rich peridotite melt produced Si-Al-Na-K-rich residual melt-I corresponding to foidolite–melilitolite. In turn, consolidation of foidolite and melilitolite resulted in Fe-Ca-C-P-F-rich residual melt-II that emplaced in silicate rocks as a phoscorite–carbonatite pipe. Crystallization of phoscorite began from forsterite, which launched destruction of silicate-carbonate-ferri-phosphate subnetworks of melt-II, and further precipitation of apatite and magnetite from the pipe wall to its axis with formation of carbonatite melt-III in the pipe axial zone. This petrogenetic model is based on petrography, mineral chemistry, crystal size distribution and crystallochemistry of forsterite. Marginal forsterite-rich phoscorite consists of Fe²⁺-Mn-Ni-Ti-rich forsterite similar to olivine from peridotite, intermediate low-carbonate magnetite-rich phoscorite includes Mg-Fe³⁺-rich forsterite, and axial carbonate-rich phoscorite and carbonatites contain Fe²⁺-Mn-rich forsterite. Incorporation of trivalent iron in the octahedral M1 and M2 sites reduced volume of these polyhedra; while volume of tetrahedral set has not changed. Thus, trivalent iron incorporates into forsterite by schema $(3\text{Fe}^{2+})_{\text{oct}} \rightarrow (2\text{Fe}^{3+} + \square)_{\text{oct}}$ that reflects redox conditions of the rock formation resulting in good agreement between compositions of apatite, magnetite, calcite and forsterite.

Keywords: forsterite; typochemistry; crystal structure; Kovdor phoscorite–carbonatite complex

1. Introduction

Phoscorite and carbonatite are igneous rocks genetically affined with alkaline massifs [1]. Many (phoscorite)-carbonatite complexes contain economic concentrations of REE (Bayan Obo, Cummins Range, Kovdor, Maoniuping, Mt. Pass, Mt. Weld, Mushgai Khudag, Tomtor, etc.), P (Catalão, Jacupiranga, Palabora, Kovdor, Seligdar, Sokli, Tapira, etc.), Nb (Araxá, Catalão, Fen, Lueshe, Mt. Weld, Oka, Panda Hill, St. Honoré, Tomtor, etc.), Cu (Palabora), Fe (Kovdor, Palabora, etc.), Zr (Kovdor, Palabora, etc.), U (Araxá, Palabora, etc.), Au, PGE (Catalão, Ipanema, Palabora, etc.), F (Amba Dongar, Maoniuping, etc.) with considerable amounts of phlogopite, vermiculite, calcite and dolomite [2–8]. The Kovdor

phoscorite–carbonatite complex in the Murmansk Region (Russia) has large resources of Fe (as magnetite), P (as hydroxylapatite), Zr and Sc (as baddeleyite), and also contains forsterite, calcite, dolomite, pyrochlore and copper sulfides with potential economic significance. Early, we have described in detail the geology and petrography of the Kovdor phoscorite–carbonatite complex [9,10] and the main economic minerals: magnetite, apatite and baddeleyite [11–13]. In this series of articles, we would like to show results of our study of potential economic minerals, namely forsterite, sulfides and pyrochlore.

Phoscorite is a rock composed of magnetite, olivine and apatite and is usually associated with carbonatites [1]. Between the phoscorite and carbonatite, there are both gradual transitions (when carbonate content in phoscorite exceeds 50 modal % the rock formally obtains name carbonatite [1]) and sharp contact (carbonatite veins in phoscorite). However, temporal relations between rocks of marginal and internal parts of phoscorite–carbonatite complexes as well as the processes that caused formation of such zonation are still unclear. The mechanism of formation of phoscorite–carbonatite rock series is widely discussed (see reviews e.g., in [8,14–19]). Most of researchers believe that phoscorite as a typical rock occurring «... around a core of carbonatite» is a result of a separate magmatic event preceding carbonatite magmatism (e.g., [20–22]). Some researchers suggest that carbonate-free phoscorite enriched by apatite and silicates (mainly forsterite) is the earlier rock in this sequence, while later carbonate-rich phoscorite and phoscorite-related carbonatite (i.e., the same phoscorite with carbonate content above 50 vol %) are formed due to the reaction between phosphate-silicate-rich phoscorite and carbonate-rich fluid or melt [21,23–28]. Some researchers divide phoscorite–carbonatite process into numerous separate intrusive events. They mainly substantiate their approach with the presence of sharp contacts between the rock varieties [29,30].

We believe that 3D mineralogical mapping is the best way to reconstruct genesis of any geological complex including phoscorite–carbonatite. This approach enabled us to establish a clear concentric zonation of the Kovdor phoscorite–carbonatite complex in terms of content, composition and properties of all economic minerals [11,13,24]. In general, the pipe marginal zone consists of (apatite)-forsterite phoscorite carrying fine grains of Ti-rich magnetite (with exsolution lamellae of ilmenite), FeMg-bearing hydroxylapatite and FeSi-bearing baddeleyite; the intermediate zone contains carbonate-free magnetite-rich phoscorite with medium to coarse grains of MgAl-bearing magnetite (with exsolution inclusions of spinel), pure hydroxylapatite and baddeleyite; and the axial zone of carbonate-rich phoscorite and phoscorite-related carbonatite includes medium- to fine-grained Ti-rich magnetite (with exsolution inclusions of geikielite–ilmenite), Sr-Ba-REE-bearing hydroxylapatite and Sc-Nb-bearing baddeleyite [11].

Consequently, phoscorite and phoscorite-related carbonatite of the Kovdor alkaline-ultrabasic massif consist of four main minerals belonging to separate classes of compounds: silicate–forsterite, phosphate–apatite, oxide–magnetite and carbonate–calcite, which compositions do not intercross (besides Ca in calcite and apatite and Fe in olivine and magnetite). Therefore, we can use content, composition and grain-size distribution, etc. of apatite for phosphorus behavior analysis, magnetite characteristics for iron and oxygen activity estimation, and forsterite and calcite characteristics for silicon and carbon evolution studies.

Forsterite can be the main key to understanding genesis and geology of the whole Kovdor alkaline-ultrabasic massif as its formation started from peridotite intrusion and finished with late carbonatites. In addition, forsterite is another economic mineral concentrated within two separate deposits [9]: the Baddeleyite-Apatite-Magnetite deposit within the phoscorite–carbonatite pipe and the Olivinite deposit within the peridotite core of the massif. For this reason, studied in details forsterite from the Kovdor phoscorite–carbonatite complex will be also compared with forsterite of the peridotite stock.

2. Geological Setting

The Kovdor massif of alkaline and ultrabasic rocks, phoscorite and carbonatites is situated in the SW of Murmansk Region, Russia (Figure 1a). It is a central-type intrusive complex with an

area of 40.5 km² at the day surface emplaced in Archean granite-gneiss [31–33]. The geological setting of the Kovdor massif has been described by [9,21,28,30,34]. The massif consists of a central stock of earlier peridotite rimmed by later foidolite (predominantly) and melilitolite (Figure 1). In cross-section, the massif is an almost vertical stock, slightly narrowing with depth at the expense of foidolite and melilitolite [35]. There is a complex of metasomatic rocks between peridotite core and foidolite–melilitolite rim: diopsidite; phlogopitite; melilite-, monticellite-, vesuvianite-, and andradite-rich skarn-like rocks. Host gneiss transforms into fenite at the distance of 0.2–2 km from the alkaline ring intrusion. Numerous dikes and veins (up to 5 m thick) of nepheline and cancrinite syenite, (micro)jijolite, phonolite, alnoite, shonkinite, calcite, calcite and dolomite carbonatites cut into all the above mentioned intrusive and metasomatic rocks [9].

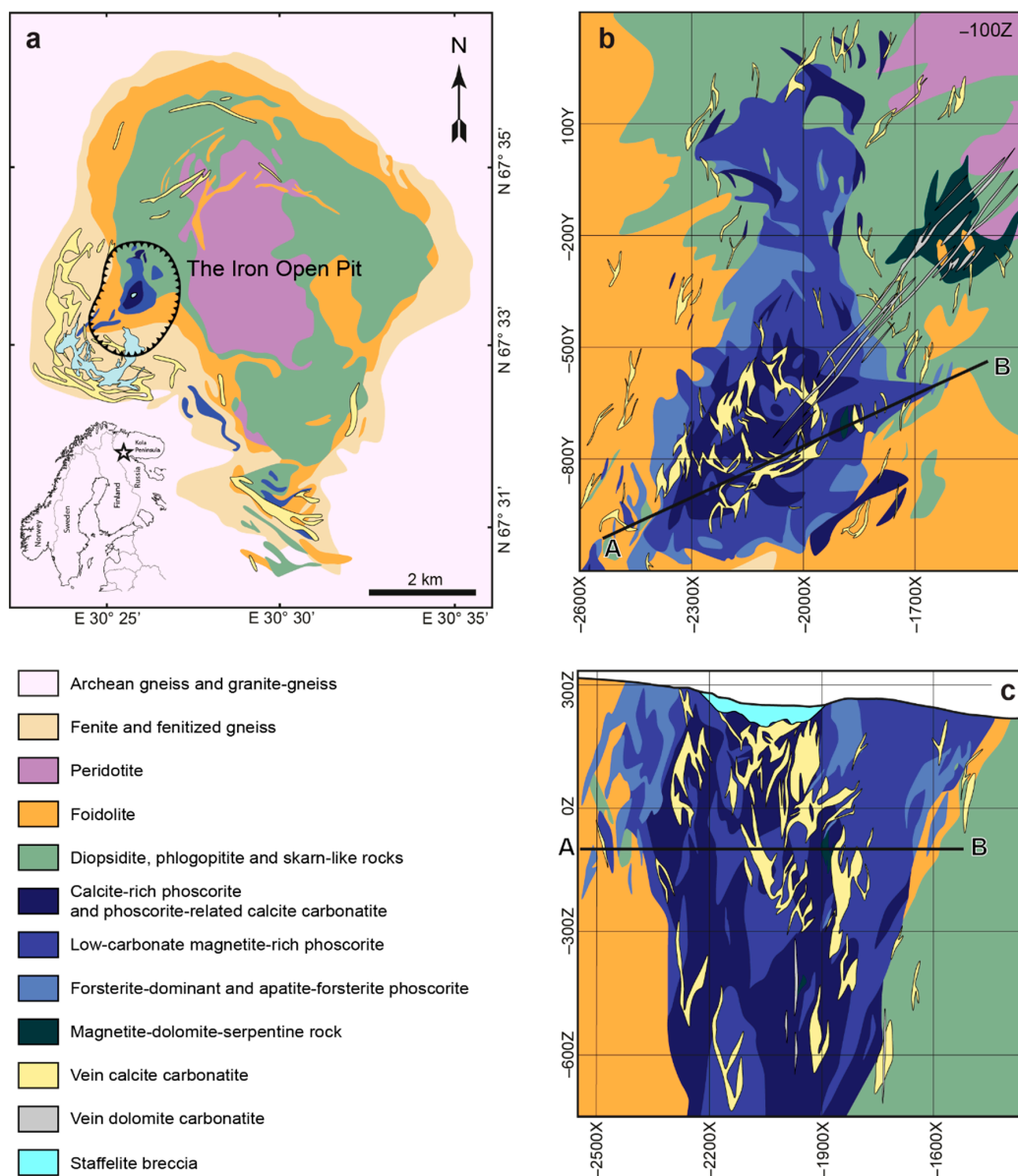


Figure 1. (a) Geological map of the Kovdor alkaline-ultrabasic massif, after Afanasyev and Pan'shin, modified after [9]; cross-sections of the Kovdor phosphorite–carbonatite complex: (b) horizontal (–100 m, Y axis shows the North) and (c) vertical along A–B line, after [11].

At the western contact of peridotite and foidolite, there is a concentrically zoned pipe of phosphorite and carbonatites (Figure 1b,c) highly enriched in magnetite, hydroxylapatite and baddeleyite.

The marginal zone of this pipe is composed of (apatite)-forsterite phoscorite (Figure 2a,b), the intermediate zone consists of low-carbonate magnetite-rich phoscorite (Figure 2c) and the axial zone contains calcite-rich phoscorite (Figure 2d) and phoscorite-related calcite carbonatite (non-vein bodies characterized by transient contact with phoscorite). Numerous carbonatite veins cut the phoscorite body, with the highest concentration of veins encountered in its axial, calcite-rich zone (Figure 1b,c and Figure 2e,g). Main varieties of phoscorite and phoscorite-related carbonatite are shown in Table 1. However, there are no distinct boundaries between these rocks, and artificial boundaries between them are quite conventional [10]. Zone of linear veins of dolomite carbonatite (Figure 1b,c) extends from the central part of the phoscorite–carbonatite pipe to the north-east and associates with metasomatic magnetite-dolomite-serpentine rock, which replaced peridotite or forsterite-rich phoscorite [9,11,24].

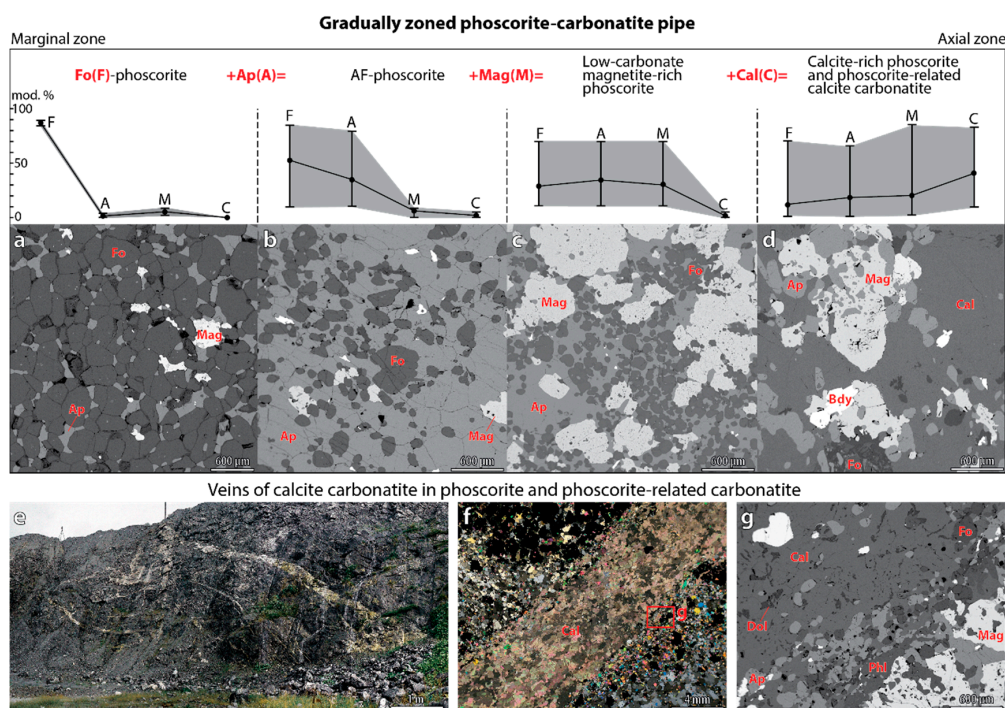


Figure 2. Relations of major rocks within the Kovdor phoscorite–carbonatite pipe. BSE-images (a–d,g) of main rock types, photo of outcrop (e) and image of thin section in transmitted light (f). (a) 914/185.2; (b) 993/132.3; (c) 981/217.1; (d) 1006/436.1; (f,g) 927/21.7.

Table 1. Main varieties of phoscorite and phoscorite-related carbonatite [10].

Group of Rock	Rock	Mineral Content, Modal %			
		Fo	Ap	Mag	Cal
Forsterite-rich phoscorite (Cal < 10 modal %, Mag < 10 modal %)	Forsterite (F)	85–90	0–5	1–8	–
	Apatite-forsterite phoscorite (AF)	10–85	10–80	0–8	0–5
Low-carbonate magnetite-rich phoscorite (Cal < 10 modal %, Mag > 10 modal %)	Magnetite-forsterite phoscorite (MF)	10–70	0–5	15–85	0–5
	Magnetite-apatite-forsterite phoscorite (MAF)	10–70	10–70	10–70	0–8
	Magnetite-apatite phoscorite (MA)	0–5	5–50	40–85	0–5
	Magnetite (M)	0–8	0–5	80–95	0–5
Calcite-rich phoscorite (10 modal % < Cal < 50 modal %)	Calcite-magnetite-apatite-forsterite phoscorite (CMAF)	10–60	10–60	10–55	10–40
	Calcite-magnetite-forsterite phoscorite (CMF)	10–70	0–5	15–60	10–45
	Calcite-apatite-forsterite phoscorite (CAF)	10–45	20–55	2–8	20–40
	Calcite-magnetite-apatite phoscorite (CMA)	0–6	10–63	11–79	10–45
	Calcite-apatite phoscorite (CA)	2–6	50–65	1–6	27–41
	Calcite-magnetite phoscorite (CM)	0–5	0–5	70–84	16–20
Phoscorite-related carbonatite (Cal > 50 modal %)	Calcite carbonatite (C)	0–35	2–40	1–35	50–82

3. Materials and Methods

For this study, we used 540 thin polished sections of phoscorite (mainly), carbonatites and host rocks from 108 exploration holes drilled within the Kovdor phoscorite–carbonatite complex. The thin polished sections were analyzed using the LEO-1450 scanning electron microscope (Carl Zeiss Microscopy, Oberkochen, Germany) with energy-dispersive analyzer Röntek to obtain BSE-images of representative regions and pre-analyze all minerals found in the samples. The ImageJ open source image processing program [36] was used to create digital images from the BSE-images, and determine forsterite grain size (equivalent circular diameter) and orientation of the grain long axis.

Chemical composition of forsterite was analyzed in the Geological Institute of the Kola Science Center, Russian Academy of Sciences, with the Cameca MS-46 electron microprobe (Cameca, Gennevilliers, France) operating in WDS-mode at 22 kV with beam diameter 10 mm, beam current 30 nA and counting times 20 s (for a peak) and 2×10 s (for background before and after the peak), with 5–10 counts for every element in each point. The analytical precision (reproducibility) of forsterite analyses is 0.2–0.05 wt % (2 standard deviations) for the major element and about 0.01 wt % for impurities. Used standards and detection limits are given in Table 2. The systematic errors are within the random errors.

Table 2. Parameters of EPMA.

Element	Type of Crystal	Standards	DL, wt %
Mg	KAP	Forsterite	0.1
Al	KAP	Pyrope	0.05
Si	KAP	Forsterite	0.05
Ca	PET	Diopside	0.03
Sc	PET	Thortveitite	0.02
Ti	PET	Lorenzenite	0.02
Cr	Quartz	Chromite	0.02
Mn	Quartz	Synthetic MnCO ₃	0.01
Fe	Quartz	Hematite	0.01
Ni	LiF	Metal nickel	0.01

n = 5–10 counts for each point (depending on dispersion).

At the X-ray Diffraction Centre of Saint-Petersburg State University, single-crystal X-ray diffraction experiments were performed on forsterite crystals 919/18.5 (1), 924/26.7 (2), 924/169.1 (3), 966/62.9 (4), 987/67.2 (5) with the Agilent Technologies Xcalibur Eos diffractometer operated at 50 kV and 40 mA. A hemisphere of three-dimensional data was collected at room temperature, using monochromatic MoK α X-radiation with frame widths of 1° and 10 s count for each frame. Crystal structures were refined in the standard setting (space group *Pnma*) by means of the *SHELX* program [37] incorporated in the *OLEX2* program package [38]. Empirical absorption correction was applied in the *CrysAlis PRO* [39] program using spherical harmonics, implemented in the *SCALE3 ABSPACK* scaling algorithm. Volumes of coordination polyhedra are calculated with the *VESTA 3* program [40]. Crystal structures were visualized with the *Diamond 3.2f* program [41].

Cation contents were calculated in the *MINAL* program by D. V. Dolivo-Dobrovolsky [42]. Statistical analyses were implemented with the *STATISTICA 8.0* [43] and *TableCurve 2D* [44] programs. Geostatistical studies and 3D modeling were conducted with the *MICROMINE 16.1* [45] program. Interpolation was performed by ordinary kriging.

Abbreviations used include Ap (hydroxylapatite), Bdy (baddeleyite), Cal (calcite), Cb (carbonate), Chu (clinohumite), Clc (clinochlore), Di (diopside), Dol (dolomite), Fo (forsterite), Mag (magnetite), Nph (nepheline), Phl (phlogopite), Po (pyrrhotite), Spl (spinel), Srp (serpentine) and Val (valleriite).

4. Results

4.1. Content, Morphology and Grain Size of Forsterite

Peridotite contains 40–90 modal % of forsterite that has rounded isometric grains (Figure 3a) up to 12 cm in diameter. Interstices within forsterite aggregate are filled with short prismatic grains of diopside (up to 50 modal %), phlogopite plates (up to 15 modal %), anhedral grains of (titano)magnetite (up to 10 modal %), and fine-granular nests of hydroxylapatite (up to 5 modal %). Within the forsterite grains, there are lens-like inclusions of diopside with skeletal or tabular crystals of relatively pure magnetite inside (Figure 3b), as well as rounded inclusions of calcite. Typical products of forsterite alteration include serpentine (lizardite and clinochrysotile), clinocllore and, rarely, clinohumite. Near the contact with foidiolite intrusion, forsterite is intensively replaced with newly formed diopside, phlogopite (Figure 3a) and richterite, up to transformation of peridotite into diopside and/or phlogopite glimmerite.

Phoscorite contains 0–90 modal % of forsterite (Figure 4a). The highest content usually occurs in marginal forsterite and apatite-forsterite phoscorite (89 and 53 modal % correspondingly, Figure 2a,b and Figure 3c,d). In intermediate low-carbonate magnetite-rich phoscorite, average content of forsterite decreases from 42 modal % in magnetite-forsterite (MF) phoscorite (Figure 3f) to 28 modal % in predominant magnetite-apatite-forsterite (MAF) phoscorite (Figures 2c and 3e), and then to 4 modal % in apatite-magnetite (AM) phoscorite and 2 modal % in magnetite (M). Average content of forsterite in axial calcite-rich phoscorite varies from 28–21 modal % in calcite-magnetite-forsterite (CMF) and calcite-magnetite-apatite-forsterite (CMAF) phoscorite (Figure 2d) to 3 modal % in calcite-magnetite-apatite (CMA) and calcite-magnetite (CM) phoscorite. Lastly, phoscorite-related carbonatite contains 5 modal % of forsterite [24].

Gradual decrease of forsterite content from earlier forsterite of the marginal zone to later carbonatites is accompanied by regular changes in morphology and grain size of forsterite as well as in its relations with other rock-forming minerals. In the marginal forsterite-rich phoscorite, forsterite forms spherical (small) to ellipsoidal (large) grains (Figure 2a,b) or, more rarely, well-shaped short prismatic crystals with $a:c = 1:1.3$. Average equivalent circular diameter of forsterite grains is 0.18 mm (Figure 4b), and grain size distribution is negative-exponential (Figure 5), when cumulative frequencies are concave down in log-log space (Figure 5d), and linear in semilog space (Figure 5c). There is insufficient anisotropy in grain orientation (Figure 5e). When forsterite content sufficiently exceeds apatite content, then hydroxylapatite fills interstices between forsterite grains. In this case, forsterite grains contain numerous inclusions of hydroxylapatite. Its content increases in the vicinity of large segregation of hydroxylapatite (Figure 3d). If the amount of hydroxylapatite increases, then spatial separation of forsterite and hydroxylapatite is observed (Figure 3e). Such monomineral segregations randomly alternate with areas evenly filled with apatite and forsterite (Figure 2b). Moreover, there are indications of co-crystallization of forsterite and hydroxylapatite. In this case, forsterite grains contain numerous inclusions of apatite and have sinuous boundaries (Figure 3c). In addition, forsterite grains sometimes contain prismatic inclusions of baddeleyite (up to 20 μm long, Figure 2f) as well as spherical inclusions (“drops”) of calcite (up to 60 μm in diameter, Figure 3c) and, rarely, dolomite (up to 20 μm in diameter). Magnetite occurs mainly within apatite segregations or fills interstices between forsterite grains together with hydroxylapatite.

In the intermediate low-carbonate magnetite-rich phoscorite, average size of forsterite grains is 0.19 mm (Figure 4b), grain size distribution is the same as in the marginal forsterite-rich phoscorite (Figure 5h,i), but without anisotropy in grain orientation (Figure 5j). Magnetite content growth leads to concentration of magnetite and forsterite in separate monomineralic nests (Figure 3f); however, hydroxylapatite still closely associates with magnetite. Forsterite grains obtain mirror-like faces at the boundary with calcite nests and veinlets. Similar to marginal (apatite)-forsterite phoscorite, forsterite grains usually contain ellipsoidal inclusions of hydroxylapatite, prismatic inclusions of baddeleyite and spherical “drops” of calcite and dolomite (Figure 3g) in the pipe intermediate zone.

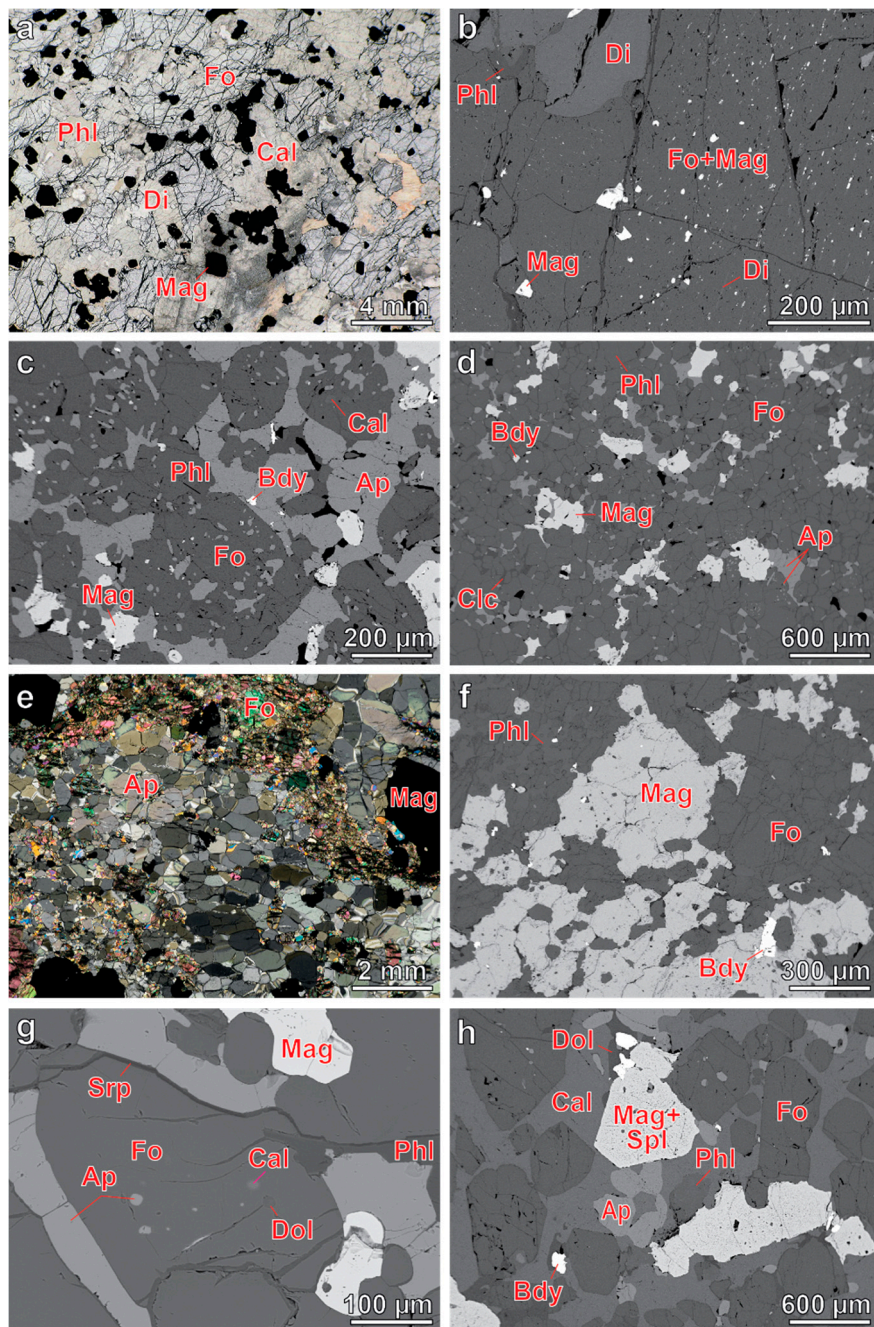


Figure 3. Morphology of forsterite and its relations with other minerals in rocks of the Kovdor alkaline-ultrabasic massif: (a) replacement of forsterite with diopside and phlogopite in peridotite 10p/76.01; (b) grain of forsterite with inclusions of diopside and magnetite in peridotite 912/231.6; (c) co-crystallization of forsterite (with inclusions of calcite) and hydroxylapatite in AF phoscorite 934/112.1; (d) interstitial segregations of magnetite and hydroxylapatite in AF phoscorite 976/33.1; (e) network of forsterite grains in MAF phoscorite 932/205.9; (f) typical MF phoscorite 983/64.6; (g) inclusions of hydroxylapatite, calcite and dolomite in forsterite grains of MAF phoscorite 938/30.6; (h) well shaped crystals of forsterite with inclusions of hydroxylapatite and calcite in CMF phoscorite 953/6.0. (a,e) images of polished thin section in transmitted light; (b–d,f–h) BSE images. Mineral abbreviations see in the Section 3.

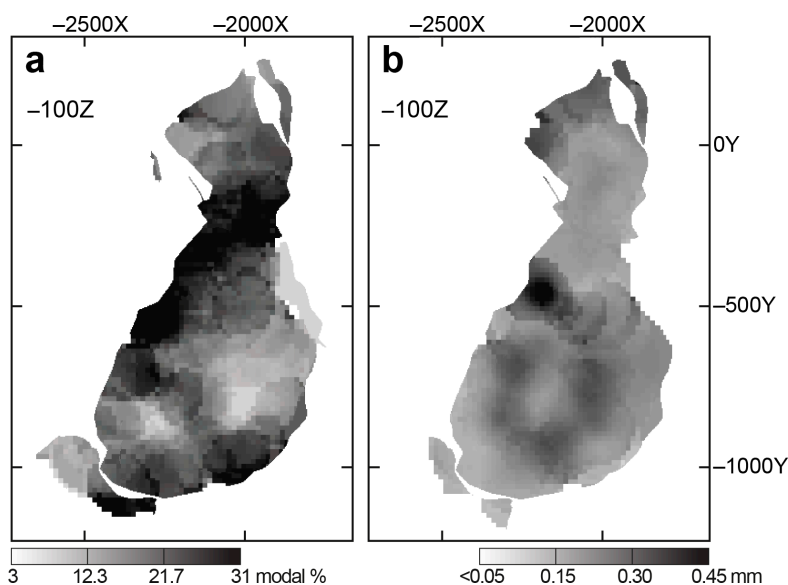


Figure 4. Distribution of forsterite content (a) and average grain size (b) within the baddeleyite-apatite-magnetite deposit.

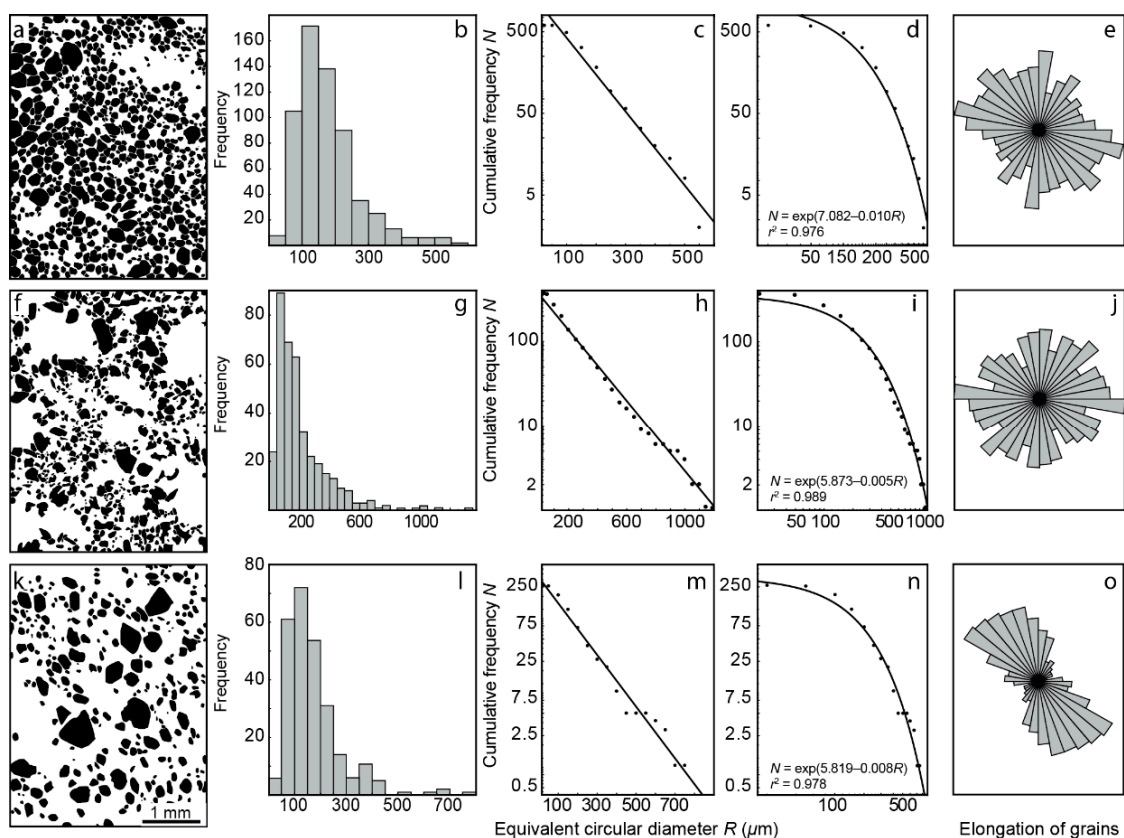


Figure 5. Grains of forsterite in thin sections of AF phoscorite 937/177.0 (a), MAF phoscorite 899/82.9 (f) and CMAF phoscorite 996/241.2 (k), corresponding histograms of equivalent circular diameter (b,g,l), cumulative frequency diagrams in semilog (c,h,m) and double logarithmic (d,i,n) coordinates, and orientation of elongated forsterite grains in the sections (e,j,o).

In the axial calcite-rich phoscorite and phoscorite-related carbonatite, minor forsterite occurs as xenomorph rounded grains within its monomineralic nests, and well-shaped short prismatic crystals

(up to 15 cm long) at the contact with calcite segregations (Figure 3h). Average size of forsterite grains is 0.2 mm (Figure 4b), grain size distribution is exponential (Figure 5m,n), and anisotropy of grain orientation is strong (Figure 5o). Inclusions in forsterite grains become rarer and smaller, and mainly consist of rounded hydroxylapatite and prismatic baddeleyite.

Vein calcite and dolomite carbonatites include only 1 modal % of small idiomorphic grains of forsterite (Figure 2g). The mineral concentrates in marginal parts of the veins intersecting forsterite-rich host phoscorite. Usually, such crystals are free of inclusions.

In all rocks of the Kovdor phoscorite–carbonatite complex, forsterite is usually partially replaced by secondary phlogopite, clinocllore, clinohumite, valleriite, serpentine, and dolomite, with clear correspondence to the pipe zonation. Apo-forsterite phlogopite occurs throughout the pipe volume; but in phoscorite-related carbonatite, it is more sparsely spread (Figure 6a). At first, mica forms polycrystalline rims around forsterite grains, and later, it forms large flexural plates with forsterite relics inside. Secondary clinocllore closely associates with phlogopite, forming rims around resorbed forsterite grains (Figure 3d), and its distribution within the phoscorite–carbonatite pipe is similar to mica (Figure 6a). Dolomite and serpentine replace forsterite predominantly within linear zone of dolomite carbonatite (Figures 2a and 6b), finally forming magnetite–dolomite–serpentine rocks after peridotite and forsterite-rich phoscorite [11,24]. Besides, serpentine associates closely with valleriite (Figure 6c), which content predictably increases in sulphide-bearing phoscorite. Apo-forsterite clinohumite occurs mainly in axial carbonate-rich phoscorite and carbonatites (Figure 6d): at first, as thin rims around forsterite grains, then, as comparatively large grains (up to 2 cm in diameter) with rare relics of forsterite.

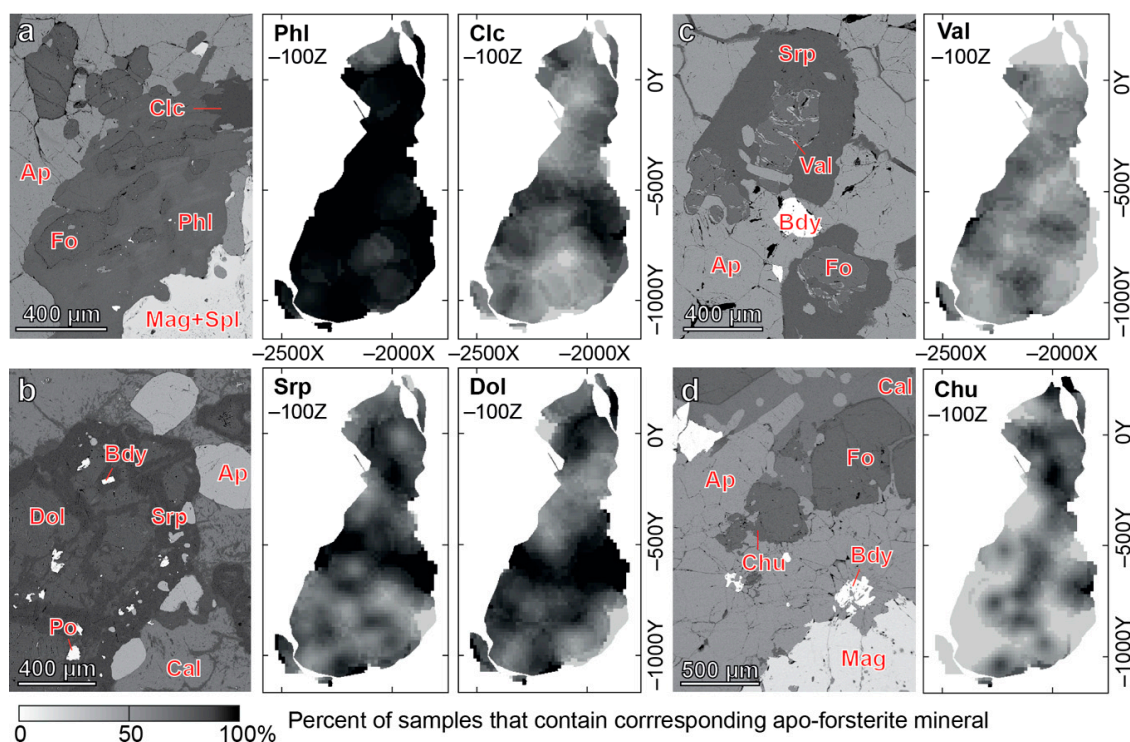


Figure 6. Relation of apo-forsterite phlogopite, clinocllore, serpentine, dolomite, valleriite and clinohumite with forsterite and distribution of these minerals within the Kovdor baddeleyite–apatite–magnetite deposit at horizon –100 m. BSE-images: (a) MAF phoscorite 992/0.9; (b) AF phoscorite 970/93.1; (c) AF phoscorite 966/165.1; (d) MAF phoscorite 986/82.2. Mineral abbreviations see in the Section 3.

4.2. Chemical Composition

Despite the long history of the Kovdor study, only 16 chemical analyzes of forsterite from this massif can be found in the literature [9,21,30,46,47]. Average data on chemical composition of forsterite are listed in Table 3. As compared with forsterite from phoscorite and carbonatites, forsterite in peridotite is relatively enriched in CaO and NiO. In the phoscorite–carbonatite complex, forsterite contains minor amounts of the substitutions; however, this is enough to define zonation of the phoscorite–carbonatite pipe. In particular, the highest content of FeO (the average content 10 wt %) characterizes forsterite from marginal (apatite)-forsterite phoscorite, the highest content of CaO (about 0.2 wt %) is predictably found in forsterite from carbonatites. The highest content of minor substitutions of TiO₂ and NiO (up to 0.07 and 0.06 wt %, correspondingly) occur in forsterite from marginal forsterite-rich phoscorite, and comparatively high content of Cr₂O₃ and Sc₂O₃ (up to 0.04 and 0.11 wt %, correspondingly) is typical for forsterite from axial calcite-rich phoscorite and phoscorite-related carbonatite. Usually, forsterite grains do not have any chemical zonation; however, some crystals of this mineral from forsterite-rich phoscorite contain iron-rich core and iron-poor marginal zone that differ by approx. 3 wt % in terms of MgO content.

Table 3. Chemical composition of forsterite (average \pm SD/min–max).

Rock	Peridotite	Phoscorite			Carbonatites	
		(Ap)-Fo	Low-Cb Mag-Rich	Cal-Rich	Phoscorite-Related	Vein
<i>n</i>	7	39	176	117	20	7
SiO ₂ , wt %	41.1 \pm 0.9 40.37–42.63	40.8 \pm 0.6 39.73–42.55	40.9 \pm 0.6 38.48–42.21	40.8 \pm 0.6 39.33–43.98	40.8 \pm 0.6 39.60–42.01	40.8 \pm 0.7 39.65–41.68
MgO	47 \pm 2 44.12–50.26	52 \pm 1 47.73–53.87	53 \pm 1 47.10–55.25	52 \pm 1 46.65–55.93	53 \pm 1 48.51–54.43	52 \pm 2 48.53–53.69
FeO	10 \pm 1 8.68–12.11	7 \pm 1 4.43–11.10	6 \pm 1 3.48–8.82	6 \pm 1 1.53–10.89	6 \pm 1 3.73–10.22	6 \pm 1 4.22–8.04
MnO	0.4 \pm 0.2 0.10–0.55	0.34 \pm 0.07 0.23–0.56	0.3 \pm 0.3 0.14–0.49	0.33 \pm 0.06 0.19–0.53	0.34 \pm 0.09 0.25–0.66	0.33 \pm 0.04 0.28–0.39
CaO	0.3 \pm 0.1 0.13–0.36	0.13 \pm 0.08 <0.03–0.40	0.12 \pm 0.08 <0.03–0.55	0.13 \pm 0.08 <0.03–0.60	0.17 \pm 0.06 0.09–0.31	0.19 \pm 0.16 0.05–0.49
TiO ₂	<0.02 <0.02–0.02	<0.02 <0.02–0.07	<0.02 <0.02–0.05	<0.02 <0.02–0.04	<0.02 <0.02–0.03	<0.02 <0.02–0.03
Al ₂ O ₃	<0.05	<0.05	<0.05	<0.05	<0.05	<0.05
Cr ₂ O ₃	<0.02 <0.02–0.03	<0.02	<0.02	\leq 0.02	<0.02 <0.02–0.04	<0.02
NiO	0.10 \pm 0.05 <0.02–0.17	<0.02 <0.01–0.06	<0.01 <0.01–0.03	<0.01 <0.01–0.03	<0.01	<0.01
Sc ₂ O ₃	<0.02	<0.02	<0.02 <0.02–0.03	<0.02 <0.02–0.11	<0.02	<0.02
Mg, <i>apfu</i>	1.75 \pm 0.06 1.66–1.82	1.87 \pm 0.04 1.77–1.92	1.89 \pm 0.03 1.74–1.95	1.89 \pm 0.04 1.75–1.99	1.89 \pm 0.03 1.79–1.93	1.88 \pm 0.04 1.8–1.93
Fe ²⁺	0.21 \pm 0.03 0.15–0.24	0.11 \pm 0.04 0.05–0.21	0.09 \pm 0.03 0.00–0.18	0.08 \pm 0.04 0.00–0.23	0.09 \pm 0.03 0.03–0.17	0.09 \pm 0.04 0.04–0.17
Fe ³⁺	0.01 \pm 0.01 0.00–0.03	0.02 \pm 0.02 0.00–0.07	0.03 \pm 0.02 0.00–0.11	0.03 \pm 0.02 0.00–0.09	0.03 \pm 0.02 0.00–0.05	0.03 \pm 0.02 0.00–0.06
Mn	0.01 0.00–0.01	0.01 0.00–0.01	0.01 \pm 0.01 0.00–0.01	0.01 0.00–0.01	0.01 0.00–0.01	0.01 0.00–0.01
Ca	0.01 0.00–0.01	0.00 0.00–0.01	0.00 0.00–0.01	0.00 0.00–0.02	0.00 0.00–0.01	0.00 0.00–0.01
Si	1.02 \pm 0.03 0.98–1.08	0.99 \pm 0.01 0.97–1.04	0.99 \pm 0.01 0.93–1.03	0.99 \pm 0.01 0.95–1.06	0.98 \pm 0.01 0.97–1.00	0.99 \pm 0.01 0.97–1.01

Forsterite composition was recalculated at three cations per formula unit and O = 4 *apfu*, which permitted to obtain more realistic results than calculations based on 3 cations per formula unit or

O = 4 *apfu* (no Fe³⁺-Fe²⁺ re-distribution), Si = 1 and O = 4 *apfu* (excess of cations in the octahedral M position), M = 2 and O = 4 *apfu* (deficit of Si). The result showed that in the average 30% of iron is in the three-valent form. There are significant correlations between Mg, Fe²⁺, Fe³⁺ and Mn ($r = \pm 0.49\text{--}0.96$, $p = 0.0000$) and weak correlations of these elements with Ca (Figure 7). Factor analysis of the cation contents (in *apfu*) was performed according to the principal components analysis with normalization and varimax rotation (Table 4). The analysis enabled us to reveal the following isomorphous substitutions:

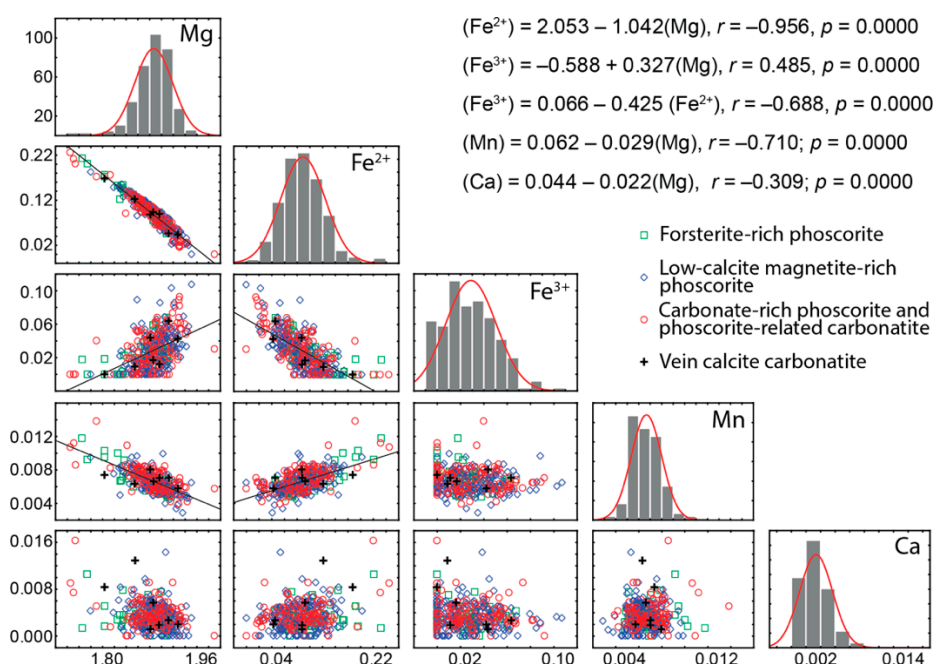
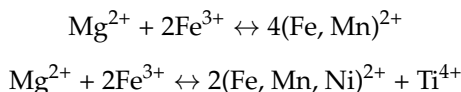


Figure 7. Matrix diagram for major octahedral cations of forsterite (*apfu*).

Table 4. Results of factor analysis of forsterite composition.

Variables	Factor Loadings	
	Factor 1	Factor 2
Mg	−0.927	−0.248
Fe ²⁺	0.961	0.179
Fe ³⁺	−0.680	−0.021
Mn	0.676	0.219
Ca	0.357	0.014
Ti	0.164	0.844
Ni	0.090	0.861
Explained variance	2.863	1.596
% of total variance	40.9	22.8

Factor loadings above 0.6 are shown in bold.

These substitutions result in clear concentric zonation of the Kovdor phoscorite–carbonatite complex in terms of forsterite composition (Figure 8). The features of forsterite composition (see above) and these figures show that the pipe marginal zone consists of Fe²⁺-Mn-Ni-Ti-rich forsterite similar to olivine from peridotite, the intermediate zone includes Mg-Fe³⁺-rich forsterite, and the axial zone contains Fe²⁺-Mn-rich forsterite. In addition, the content of Fe³⁺ in forsterite increases with depth. The tendency is accompanied by growth of Mg and Mn cumulative concentration with depth; however,

these elements themselves vary in inverse proportion to each other. Ca content in forsterite increases sufficiently in carbonate-rich rocks located deeper than -500 m.

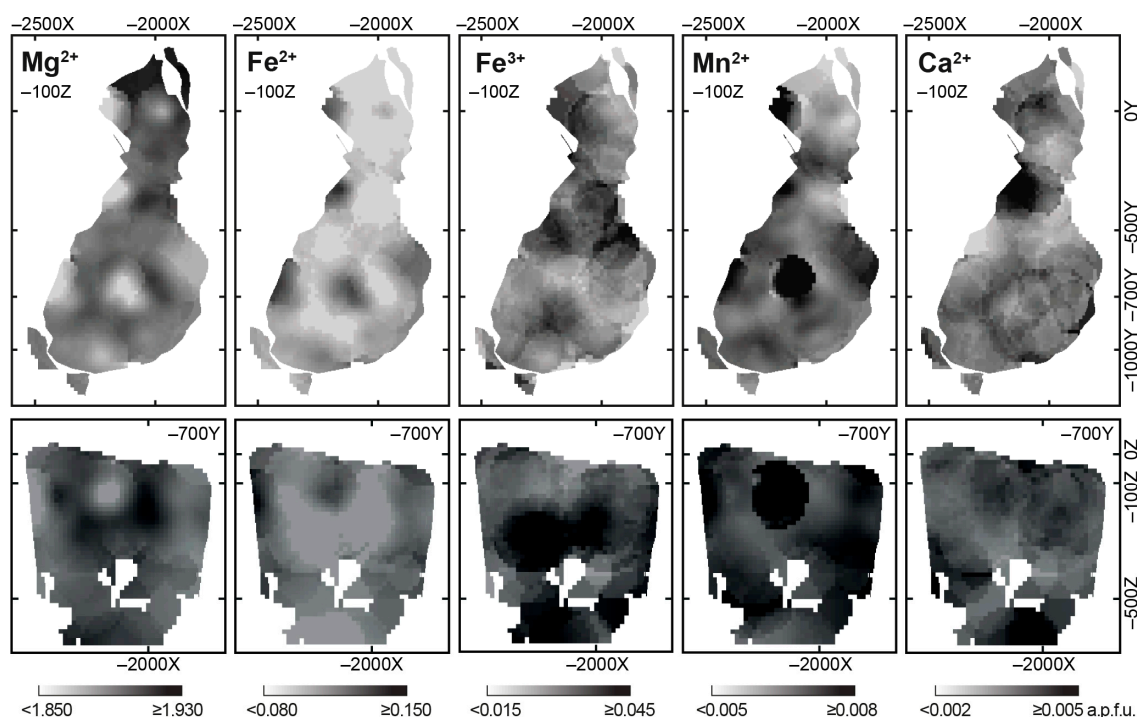


Figure 8. Variations in forsterite composition (apfu) within the Kovdor baddeleyite-apatite-magnetite deposit.

As noted earlier [9,11,13,24], chemical compositions of other minerals also change in accordance with a concentric zonation of the Kovdor phosphorite–carbonatite complex. Therefore, compositions of forsterite and other rock-forming and accessory minerals must be interdependent. Figure 9 shows correlation coefficients between main components of forsterite and co-existing rock-forming minerals. Forsterite composition closely correlates with composition of apatite, magnetite and calcite, with fundamental role of the main scheme of isomorphism, $\text{Mg}^{2+} + 2\text{Fe}^{3+} + \square \leftrightarrow 4\text{Fe}^{2+}$ that reflects redox conditions of the rock formation. In fact, oxidized condition results in presence of Fe^{3+} instead of Fe^{2+} in melt/fluid/solution, and thus in crystallization of Mg- Fe^{3+} -rich members of the corresponding mineral series, while reduced conditions cause domination of Fe^{2+} and formation of ferrous members of these series.

As a result, in marginal forsterite-rich phosphorite, predominant «ferrous forsterite» associates with Fe^{2+} -Si-rich hydroxylapatite, Mn-Si-Ti-Zn-Cr-rich magnetite, and Fe^{2+} -rich calcite. In the intermediate low-carbonate magnetite-rich phosphorite, predominant Fe^{3+} -bearing forsterite occurs together with pure hydroxylapatite, Mg-rich magnetite and pure calcite. In the axial calcite-rich phosphorite and phosphorite-related carbonatite, «ferrous forsterite» again predominates in the associations with Fe^{2+} -Mn-rich hydroxylapatite, Ca-V-rich magnetite and Fe^{2+} -rich calcite. Comparison of the maps shown in Figure 8 with the corresponding schemas for associated rock-forming minerals [11] also confirms the above conclusion.

Electron spin resonance spectroscopy performed by Zeira et al. [48] demonstrated incorporation of Fe^{3+} in forsterite structure into M1 and M2 octahedral sites. According to Janney and Banfield [49], during oxidation under acidic conditions, incorporation of Fe^{3+} into octahedral sets of olivine is compensated by vacancies in octahedral sets: $(3\text{Fe}^{2+})_{\text{oct}} \rightarrow (\square + 2\text{Fe}^{3+})_{\text{oct}}$ (lahunite schema). Under alkaline conditions, olivine oxidation is accompanied by leaching of SiO_4 -tetrahedra: $(4\text{Fe}^{2+})_{\text{oct}} + (4\text{Si}^{4+})_{\text{tet}} \rightarrow (4\text{Fe}^{3+})_{\text{oct}} + (\square + 3\text{Si}^{4+})_{\text{tet}}$. Due to permanent deficit of tetrahedral cations in forsterite (see Table 3) and alkaline nature of the Kovdor phosphorite–carbonatite complex, we assume that forsterite oxidation follows the latter schema. However, this assumption should be confirmed with X-ray crystal study.

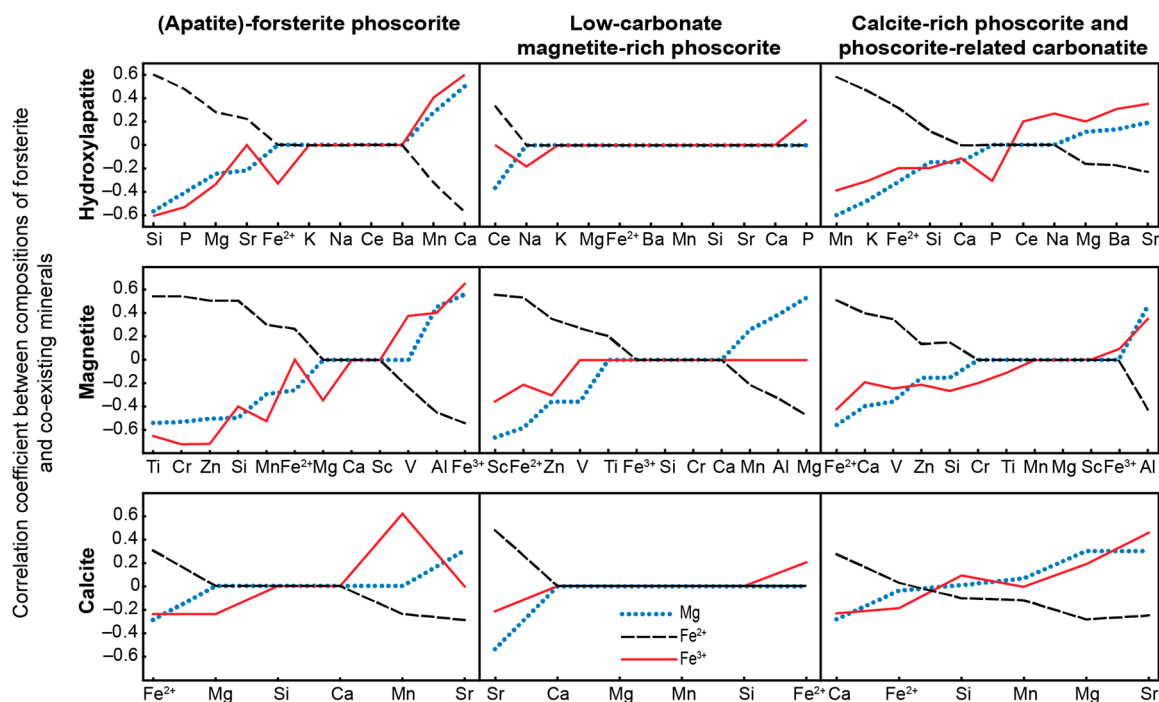


Figure 9. Correlation coefficients of forsterite composition with hydroxylapatite, magnetite and calcite compositions.

4.3. Single Crystal X-ray Diffraction

For the X-ray crystal study, we selected 5 forsterite crystals with various content of Mg, Fe^{2+} and Fe^{3+} from different zones of the phoscorite–carbonatite pipe (Table 5). The study details and crystallographic parameters obtained are shown in Table 6. Final atomic coordinates and isotropic displacement parameters selected interatomic distances and anisotropic displacement parameters are specified in the supplementary electronic materials (Tables S1–S20 in Supplementary Materials, CIF data available).

Table 5. Chemical composition of forsterite analyzed with single crystal X-ray diffraction.

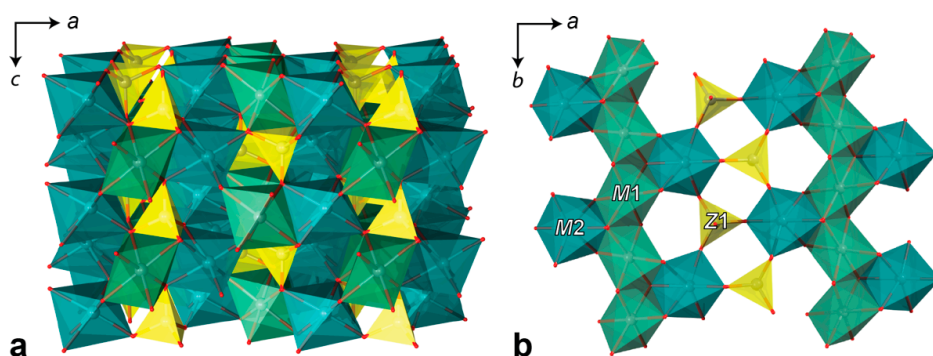
Sample	1	2	3	4	5
Drill hole	919	924	924	966	987
Depth, m	18.5	26.7	169.1	62.9	67.2
Phoscorite	Mag-Ap-Fo	Cal-Mag-Ap-Fo	Ap-Fo	Mag-Ap-Fo	Cal-Mag-Ap-Fo
SiO_2 , wt %	39.37	40.69	40.71	40.16	40.74
TiO_2	bd	0.01	0.07	bd	bd
FeO	6.20	8.96	8.51	8.42	6.89
MnO	0.30	0.46	0.49	4.27	0.39
MgO	53.37	47.79	48.96	47.10	52.18
CaO	0.13	0.34	0.06	0.14	0.09
NiO	bd	bd	0.06	bd	bd
Total	99.37	98.25	98.86	100.09	100.29
Mg, apfu	1.917	1.778	1.804	1.738	1.871
Fe^{2+}	0.022	0.187	0.176	0.163	0.098
Fe^{3+}	0.103	—	—	0.012	0.040
Mn^{2+}	0.006	0.010	0.010	0.090	0.008
Ca^{2+}	0.003	0.009	0.002	0.004	0.002
Ni^{2+}	—	—	0.001	—	—
Ti^{4+}	—	—	0.001	—	—
Si^{4+}	0.949	1.016	1.006	0.994	0.980

bd—below detection limit.

Table 6. Crystal data, data collection and structure refinement parameters of forsterite.

Sample	1	2	3	4	5
Refined formula	Mg _{1.94} Fe _{0.06} SiO ₄	Mg _{1.87} Fe _{0.13} SiO ₄	Mg _{1.84} Fe _{0.16} SiO ₄	Mg _{1.89} Fe _{0.11} SiO ₄	Fe _{0.10} Mg _{1.90} SiO ₄
Temperature/K			293(2)		
Crystal system			orthorhombic		
Space group			<i>Pnma</i>		
<i>a</i> , (Å)	10.1899(6)	10.2165(4)	10.2097(4)	10.2027(4)	10.1980(4)
<i>b</i> , (Å)	5.9730(4)	5.9911(2)	5.9876(3)	5.9775(3)	5.9810(2)
<i>c</i> , (Å)	4.7403(3)	4.76168(14)	4.7600(2)	4.7541(2)	4.75403(16)
$\alpha = \beta = \gamma$, (°)	90	90	90	90	90
Volume, (Å ³)	288.51(3)	291.453(18)	290.99(2)	289.94(2)	289.970(18)
<i>Z</i>	4	4	4	4	4
ρ_{calc} , (g/cm ³)	3.279	3.298	3.331	3.299	3.299
μ /mm ^{−1}	1.321	1.639	1.813	1.544	1.544
Crystal size, (mm ³)	0.23 × 0.18 × 0.16	0.27 × 0.21 × 0.18	0.29 × 0.25 × 0.16	0.18 × 0.15 × 0.14	0.19 × 0.17 × 0.16
Radiation			MoK α (λ = 0.71073)		
2 θ range for data collection, (°)	7.99–54.916	7.978–54.914	7.984–54.942	7.99–54.844	7.992–54.86
Index ranges	−13 ≤ <i>h</i> ≤ 11, −7 ≤ <i>k</i> ≤ 4, −6 ≤ <i>l</i> ≤ 5	−13 ≤ <i>h</i> ≤ 5, −4 ≤ <i>k</i> ≤ 7, −6 ≤ <i>l</i> ≤ 5	−13 ≤ <i>h</i> ≤ 3, −6 ≤ <i>k</i> ≤ 7, −6 ≤ <i>l</i> ≤ 3	−13 ≤ <i>h</i> ≤ 9, −6 ≤ <i>k</i> ≤ 7, −5 ≤ <i>l</i> ≤ 6	−6 ≤ <i>h</i> ≤ 13, −5 ≤ <i>k</i> ≤ 7, −6 ≤ <i>l</i> ≤ 3
Reflections collected	725 361	755 364	794 364	753 363	738 363
Independent reflections	[<i>R</i> _{int} = 0.0222, <i>R</i> _{sigma} = 0.0333]	[<i>R</i> _{int} = 0.0161, <i>R</i> _{sigma} = 0.0228]	[<i>R</i> _{int} = 0.0291, <i>R</i> _{sigma} = 0.0414]	[<i>R</i> _{int} = 0.0212, <i>R</i> _{sigma} = 0.0290]	[<i>R</i> _{int} = 0.0149, <i>R</i> _{sigma} = 0.0214]
Data/restraints/parameters	361/0/42	364/0/36	364/0/42	363/0/42	363/0/42
Goodness-of-fit on F ²	1.040	1.146	1.077	1.149	1.253
Final <i>R</i> indexes	<i>R</i> ₁ = 0.0334, [<i>I</i> > 2 σ (<i>I</i>)] <i>wR</i> ₂ = 0.0852	<i>R</i> ₁ = 0.0274, <i>wR</i> ₂ = 0.0713	<i>R</i> ₁ = 0.0260, <i>wR</i> ₂ = 0.0593	<i>R</i> ₁ = 0.0239, <i>wR</i> ₂ = 0.0602	<i>R</i> ₁ = 0.0258, <i>wR</i> ₂ = 0.0683
Final <i>R</i> indexes [all data]	<i>R</i> ₁ = 0.0359, <i>wR</i> ₂ = 0.0873	<i>R</i> ₁ = 0.0283, <i>wR</i> ₂ = 0.0722	<i>R</i> ₁ = 0.0336, <i>wR</i> ₂ = 0.0634	<i>R</i> ₁ = 0.0261, <i>wR</i> ₂ = 0.0619	<i>R</i> ₁ = 0.0273, <i>wR</i> ₂ = 0.0690
Largest diff. peak/hole, (e/Å ^{−3})	0.57/−0.55	0.53/−0.69	0.50/−0.48	0.47/−0.60	0.46/−0.65

Forsterite crystal structure (Figure 10a) was firstly described by Bragg and Brown [50]. Ideally, it consists of a hexagonal close packing of oxygen atoms, where one-half of octahedral interstices is occupied by M1 and M2 sites and one-eighth of tetrahedral interstices is occupied by Z1 sites. This structure can be described as heteropolyhedral framework consisting of stacking of identical sheets parallel to the (001) plane. The sheets, in turn, are based upon chains of edge-sharing M1 octahedra with adjacent M2 octahedra connected by vertex-shared Z1 tetrahedra (Figure 10b).

**Figure 10.** Crystal structure of forsterite (1): a general view (a) and heteropolyhedral sheet based on M1, M2 octahedra (green) and Z1 tetrahedra (yellow) projected along *c* axis (b).

There are few reports on non-equivalent distribution of magnesium and iron at octahedral M1 and M2 positions of the olivine-type structure [51–54]. This type of cation ordering does not reveal a correlation between cation distribution and genesis of the crystals, which is typical for amphiboles and pyroxenes [53,55,56]. In all forsterite analyzed, refined occupations of M1 and M2 sites provide domination of iron at the “large” M2 site (Table 7, Figure 11a). From the crystal-chemical point of view,

the substitution $M^2Mg^{2+} \rightarrow M^2Fe^{2+}$ is more reasonable than $M^1Mg^{2+} \rightarrow M^1Fe^{2+}$ because the observed $\langle M2-O \rangle$ bond lengths of 2.128–2.135 Å are closer to ideal $\langle Fe^{2+}-O \rangle$ distance of 2.180 Å [57] than to $\langle M1-O \rangle$ distances (2.091–2.099 Å). For the same reason, M1 site is theoretically more suitable for incorporation of Fe^{3+} (ideal $\langle Fe^{3+}-O \rangle$ bond length is 2.045 Å).

Table 7. Refined iron content of octahedral M1 and M2 sites for 1–5 samples (apfu).

Sample	M1	M2
1	0.020	0.035
2	0.057	0.070
3	0.080	0.084
4	0.047	0.057
5	0.04	0.065

The average $\langle M-O \rangle$ distances increase statistically irregularly with increasing content of Fe^{2+} (Figure 11b), which results in alignment of “small” M1 and “large” M2 octahedra in the Fo–Fa series (the average $\langle M1-O \rangle$ and $\langle M2-O \rangle$ distances are 2.094 and 2.130 Å correspondingly in forsterite, and 2.161 and 2.179 Å correspondingly in fayalite [58]). In case of sufficient difference between ionic radii of Mg^{2+} and incorporated elements [e.g., Fe^{3+} (−10.4%) or Mn^{2+} (+15.3%)], trivalent iron occupies firstly “large” M2 site, and Mn^{2+} incorporates into “small” M1 site [59,60]. Since the most significant difference in sizes of M1 and M2 polyhedra is observed in forsterite $Fo_{1.00}$ – $Fo_{0.8}Fa_{0.2}$, incorporation of Fe^{3+} at the octahedral sites will have maximum impact on the M1 and M2 polyhedra volume in such forsterites.

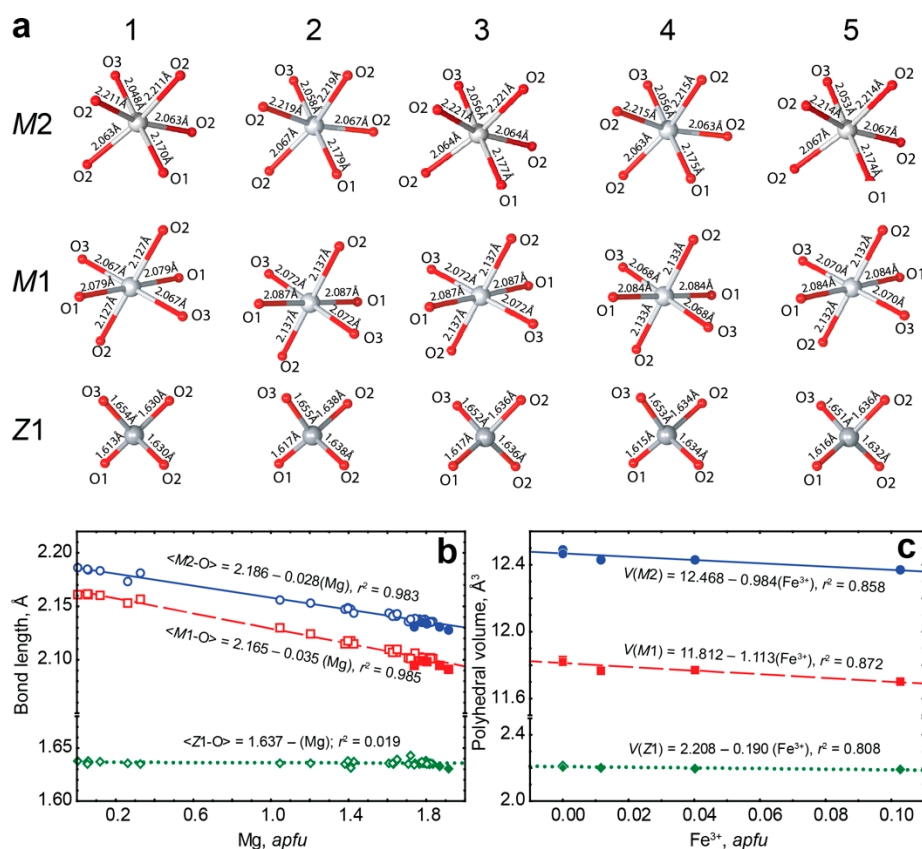


Figure 11. Geometry of coordination polyhedra in crystal structure of forsterites 1–5 (a), scatterplot of average $\langle M1-O \rangle$, $\langle M2-O \rangle$ and $\langle Z1-O \rangle$ bond lengths against magnesium content in olivine according to [61–64], and present data (filled squares and circles) (b), scatterplot of polyhedral volumes (M1, M2 and Z1) against ferric iron content (c).

In crystal structure of Kovdor's forsterite, the average $\langle Z1-O \rangle$ distances range between 1.631–1.637 Å, and scattering factors of Z1 sites vary in the range of 13.30–14.00 electrons per formula unit, which is in good agreement with full occupation of Z1 site by Si atoms only (Figure 11a). Polyhedral volumes of Z1 tetrahedra are actually unchanged, and this fact does not confirm incorporation of Fe^{3+} into tetrahedral sites (Figure 11c). The polyhedral volume decreasing with growth of Fe^{3+} content in our samples confirms incorporation of trivalent iron into octahedral M1 and M2 sites via laihulite-like substitution $(3Fe^{2+})_{oct} \leftrightarrow (2Fe^{3+} + \square)_{oct}$. Unconstrained refinement of forsterites with significant amounts of Fe^{3+} (samples 1 and 5) with full occupancies of octahedral (M11.00, M21.00) sites results in significant underestimation of Fe content. This fact also proves presence of vacancies at octahedral sites only. Consequently, data of crystal structure refinement is in good agreement with factor analysis and chemical data. Presence of vacancies at octahedral sites of partially “oxidized” olivine questions applicability of distribution coefficients KD and associated variables [53,65,66].

5. Discussion

We would like to express that forsterite from peridotite has an important feature—bimineral exsolution lamellae of magnetite and diopside (Figures 3b and 12b). Such lamellae are not found in forsterite from phoscorite and carbonatites of the Kovdor alkaline-ultrabasic massif; but they are common in other (ultra)basic complexes where forsterite is enriched in Fe^{2+} and Ca [67,68]. In turn, Ca-rich forsterite crystallizes from melt with relatively low mg# value $MgO/(MgO + FeO)$ and high contents of Ca and Na [69]. The fact that ultrabasic melt of the Kovdor massif was enriched in Ca is confirmed by co-crystallization of forsterite and diopside as well as by presence of numerous calcite inclusions (“drops”) within forsterite grains (Figure 12b). In addition, Ca-rich foidolite (Figure 2d) and melilitholite formed later than peridotites contain calcite “drops” inside grains of all the main minerals including nepheline [24]. Low value of mg# in this melt causes crystallization of titanomagnetite in interstices of olivine grains (Figure 3a) up to formation of magnetite-rich peridotite (see Figure 1) that have economic importance [9].

Alkaline melts have relatively higher $Fe^{3+}/(Fe^{3+} + Fe^{2+})$ ratio, than non-alkaline melts [70,71], and Fe^{3+} is partly included in forsterite. The rock cooling causes exsolution of Fe^{3+} -rich forsterite into diopside and magnetite [72]:

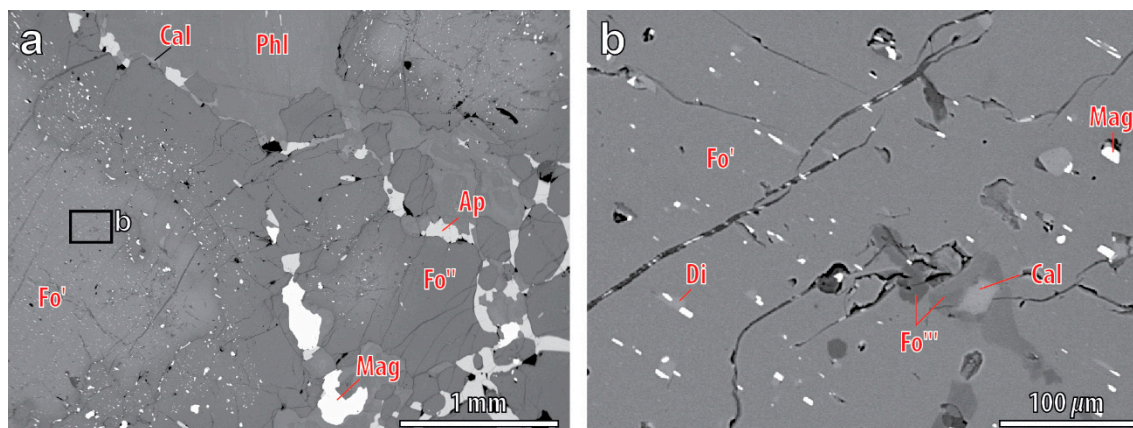
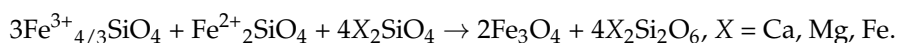


Figure 12. BSE-images of a rim of newly formed “phoscoritic” forsterite-II ($Fo'' = Fo_{92}Fa_8$) around relict grain of “peridotitic” forsterite-I ($Fo' = Fo_{93}Fa_7$) in AF-phoscorite 937/114.6 (a) and the enlarged region demonstrating diopside lamellae and calcite “drops” in forsterite (b). $Fo''' = Fo_{95}Fa_5$. Other mineral abbreviations see in the Section 3.

The pyroxene phase acts as a sink for elements not compatible with the olivine structure, such as Ca. Pyroxene is formed as long as there is sufficient Ca present and the temperature is high enough for it to diffuse to the reaction front.

After crystallization of forsterite and diopside in peridotite, residual melt (melt-I) became comparatively rich in Si, Al, Na and K [21,73]. The melt-I emplaced into contact zone between peridotite stock and host gneisses and formed ring of foidolite and melilitolite. The next residual melt-II contained insignificant amount of Si (and Mg), but it was strongly enriched in Fe, Ca, C, P, F and also Nb, Zr, REE, Th and U. So, it was a real residual melt that was not caused by liquid immiscibility, because «ore-bearing rare metal carbonatites that are found in association with ultramafic and alkaline silicate rocks are likely to have formed from a residual liquid after extensive fractional crystallization of carbonated silicate magma rather than by silicate–carbonate liquid immiscibility» [74]. The possible existence of carbonatite magmas was experimentally confirmed in the system CaO–CO₂–H₂O by Wyllie and Tuttle [75]. There were discovered the liquid immiscibility between albite-rich silicate and sodium carbonate-rich liquids [76,77], between ijolitic and alkali carbonatitic liquids in experiments on whole-rock compositions [78], and between alkali-poor silicate and carbonate liquids in the system albite/anorthite–calcite [79,80]. Studies in NaAlSi₃O₈–NaAlSiO₄–CaCO₃–H₂O system by [81] and in Mg₂SiO₄–CaCO₃–Ca(OH)₂ system by [82,83] indicated that carbonatite magmas could be produced by crystal fractionation of silicate magmas of appropriate compositions (for example, SiO₂-undersaturated alkalic liquids with H₂O and CO₂). For other compositions, this is precluded by the presence of thermal barriers between high-temperature liquids precipitating silicates, and low-temperature liquids precipitating carbonates and hydrous minerals [82,83]. Reasons of phosphorus concentration in the residual melt-II include enrichment of the melt in Fe³⁺ with further formation of stable complex Fe³⁺(PO₄)^{3−} [84,85] as well as high content of Ca and Mg forming stable complexes (Ca, Mg)–PO₄ [86]. We believe that residual melt-II intruded into the foidolite–peridotite contact, and rapidly crystallized from the pipe walls towards its axial zone due to both cooling and blast-like degassing [24]. On this reason, hydroxylapatite co-crystallized with forsterite contains numerous liquid-vapor inclusions [87].

The crystallization of phoscorite–carbonatite rock series can be considered in systems that are extensions of well-studied CaO–CO₂–H₂O [75]. The crystallization of apatite from low-temperature melts in CaO–CaF₂–P₂O₅–H₂O and CaO–P₂O₅–CO₂–H₂O systems was investigated by Biggar [88]. There is a large field for the primary crystallization of apatite in the ternary systems Ca₃(PO₄)₂–CaF₂–Ca(OH)₂ and Ca₃(PO₄)–CaCO₃–Ca(OH)₂, and the liquid precipitating the apatite persists down to 675 °C and 654 °C at the respective ternary eutectics [89]. Addition of other components to the system CaO–CO₂–H₂O produces suitable conditions for the crystallization of other calcium-bearing minerals from low-temperature liquids in the presence of an aqueous vapor phase. Fields for the crystallization of hydrated and carbonated calcium silicates are found in the system CaO–SiO₂–CO₂–H₂O [90].

According to Moussallam et al. [91], silica and carbonate form two separate subnetworks. Phosphorus in silicate melts also forms separate clusters that confine iron within stable complexes Fe³⁺(PO₄) [86]. It seems likely that structure of the phoscorite melt was constituted by interconnected subnetworks of SiO₄-tetrahedra and CO₃-triangles with local domains of PO₄-tetrahedra and Fe³⁺(PO₄)-clusters, without a liquid immiscibility [92]. Interaction of this melt with silicate rock launched forsterite crystallization, sometimes with grains of primary “peridotitic” forsterite as seed crystals (Figure 12a). Exponential distribution of forsterite grain size (see Figure 5) shows slower diffusion rates of magnesium and silica, which seems to be the main factor of size-independent (constant) crystal growth [93]. At the contact with the carbonates (predominantly calcite), forsterite grains of phoscorite and phoscorite-related carbonatite became larger (see Figure 4b) and well-shaped (see Figure 3h) due to collective recrystallization. Similar processes are typical for magnetite [12].

Crystallization of forsterite from residual melt-II near the pipe wall and top resulted in depletion of the melt in Mg, which launched apatite precipitation with the melt cooling. In turn, formation of apatite destroyed Fe³⁺(PO₄)-complexes and launched magnetite crystallization. Consequently,

crystallization front moved rapidly from the pipe wall towards its axis accompanied by separation of volatiles. This process resulted in concentration of residual carbonate melt-III in the pipe axial zone.

Carbonate melts are low-viscous and remain interconnected up to 0.05 wt % melt [94]. In addition, silicate melt selectively wets the grain-edge channels between solid phases, excluding the carbonate melt to the center of melt pockets, away from grain edges [95]. These features of carbonate melts enable us to understand why forsterite grains can crystallize from carbonate-rich melt according to low-rate diffusion mechanism, and why they obtain predominant orientation in carbonate melt flow (see Figure 5).

Water solubility in carbonate melts is significantly higher than in alkaline silicate melts, reaching values of nearly 15 wt % at 100 MPa and 900 °C [96]. The depth of –200 to –400 m is probably the interval of separation of water, CO₂, F and other volatiles from phoscorite–carbonatite melt. These volatiles reacted with early crystallized phoscorites and phoscorite-related carbonatites in the pipe axial zone, with formation of later water/fluor-containing apo-forsterite minerals (phlogopite, clinocllore, clinohumite, etc.—see Figure 6). The final products of this process were staffelite breccias (fragments of altered phoscorite and carbonatites cemented by colloform carbonate-rich fluorapatite) filling several funnels in apical part of the phoscorite–carbonatite pipe axial zone [24,97].

6. Conclusions

Three-D mineralogical mapping was used to establish spatial distribution of forsterite content, morphology, grain size, composition and alteration products within the Kovdor phoscorite–carbonatite pipe. This work pursues our study of “through minerals” of the Kovdor complex and enables us to make some interesting conclusions:

- (1) Forsterite is the earliest mineral of both peridotite and phoscorite–carbonatite complexes, and its crystallization governed the further evolution of corresponding magmatic systems. Thus, crystallization of forsterite from the Ca-Fe-rich peridotite melt produces Si-Al-Na-K-rich residual melt-I corresponding to foidolite–melilitolite. In turn, consolidation of foidolite and melilitolite produced Fe-Ca-C-P-F-rich residual melt-II that emplaced in silicate rocks as the phoscorite–carbonatite pipe. Phoscorite crystallization started from forsterite, which launched destruction of silicate-carbonate-ferriphosphate subnetworks of the melt followed by precipitation of apatite and magnetite from the pipe wall to its axis with formation of carbonatite melt-III in the pipe axial zone;
- (2) Growth of forsterite grains from phoscorite–carbonatite melt was diffusion-limited, which causes constant growth rate of each grain and exponential distribution of grain size;
- (3) Chemical composition of forsterite in phoscorite–carbonatite pipe is determined by two schemas of isomorphism: $\text{Mg}^{2+} + 2\text{Fe}^{3+} \leftrightarrow 4(\text{Fe}, \text{Mn})^{2+}$ and $\text{Mg}^{2+} + 2\text{Fe}^{3+} \leftrightarrow 2(\text{Fe}, \text{Mn}, \text{Ni})^{2+} + \text{Ti}^{4+}$. Marginal forsterite-rich phoscorite consists of Fe²⁺-Mn-Ni-Ti-rich forsterite similar to olivine from peridotite, intermediate low-carbonate magnetite-rich phoscorite includes Mg-Fe³⁺-rich forsterite, and axial carbonate-rich phoscorite and carbonatites contain Fe²⁺-Mn-rich forsterite;
- (4) Trivalent iron incorporates into forsterite by scheme $(3\text{Fe}^{2+})_{\text{oct}} \rightarrow 2\text{Fe}^{3+} + (\square)_{\text{oct}}$ that reflects redox conditions of the rock formation causing significant agreement between compositions of apatite, magnetite, calcite and forsterite;
- (5) Incorporation of trivalent iron at the octahedral M1 and M2 sites decreases the volume of these polyhedra, while volume of tetrahedral set does not change. Thus, the assumed substitution $(4\text{Fe}^{2+})_{\text{oct}} + (4\text{Si}^{4+})_{\text{tet}} \rightarrow (4\text{Fe}^{3+})_{\text{oct}} + (3\text{Si}^{4+} + \square)_{\text{tet}}$ proposed by D. E. Janney and J. F. Banfield [49] was not confirmed. Our data show that laihunite-like isomorphism is more common in forsterite than it was considered to be.

Supplementary Materials: The following are available online at <http://www.mdpi.com/2075-163X/8/6/260/s1>, Table S1: Fractional atomic coordinates ($\times 10^4$) and equivalent isotropic displacement parameters ($\text{\AA}^2 \times 10^3$) for Forsterite_1. Table S2: Anisotropic displacement parameters ($\text{\AA}^2 \times 10^3$) for Forsterite_1. Table S3: Bond

lengths for Forsterite_1, Table S4: Atomic occupancy for Forsterite_1, Table S5: Fractional atomic coordinates ($\times 10^4$) and equivalent isotropic displacement parameters ($\text{\AA}^2 \times 10^3$) for Forsterite_2, Table S6: Anisotropic displacement parameters ($\text{\AA}^2 \times 10^3$) for Forsterite_2, Table S7: Bond lengths for Forsterite_2, Table S8: Atomic occupancy for Forsterite_2, Table S9: Fractional atomic coordinates ($\times 10^4$) and equivalent isotropic displacement parameters ($\text{\AA}^2 \times 10^3$) for Forsterite_3, Table S10: Anisotropic displacement parameters ($\text{\AA}^2 \times 10^3$) for Forsterite_3, Table S11: Bond lengths for Forsterite_3, Table S12: Atomic occupancy for Forsterite_3, Table S13: Fractional atomic coordinates ($\times 10^4$) and equivalent isotropic displacement parameters ($\text{\AA}^2 \times 10^3$) for Forsterite_4, Table S14: Anisotropic displacement parameters ($\text{\AA}^2 \times 10^3$) for Forsterite_4, Table S15: Bond lengths for Forsterite_4, Table S16: Atomic occupancy for Forsterite_4, Table S17: Fractional atomic coordinates ($\times 10^4$) and equivalent isotropic displacement parameters ($\text{\AA}^2 \times 10^3$) for Forsterite_5, Table S18: Anisotropic displacement parameters ($\text{\AA}^2 \times 10^3$) for Forsterite_5, Table S19: Bond lengths for Forsterite_5, Table S20: Atomic occupancy for Forsterite_5.

Author Contributions: J.A.M. designed the experiments, carried out petrographical investigations and crystal size distribution analyses, and wrote the manuscript. G.Y.I. designed the experiments, performed statistical investigations, and reviewed the manuscript. A.O.K. performed geostatistical investigation, drew maps and took samples. Y.A.P. and A.V.B. took BSE images and performed electron microscope investigations. T.L.P. performed crystallographic investigations and formulated crystal-chemical conclusions. V.N.Y. and N.G.K. conceived of the work, took and prepared samples. P.M.G. drew maps. All authors discussed the manuscript.

Funding: The research is supported by the Russian Science Foundation, grant 16-17-10173.

Acknowledgments: Samples were taken during exploration of deep levels of the Kovdor deposit implemented by JSC Kovdorskiy GOK in 2007–11. X-ray crystal studies were carried out with the equipment provided by the X-ray Diffraction Centre of Saint-Petersburg State University. The comments by anonymous reviewers helped us to significantly improve this paper.

Conflicts of Interest: The authors declare no conflict of interest. The founding sponsors had no role in the design of the study; in the collection, analyses, or interpretation of data; in the writing of the manuscript, and in the decision to publish the results.

References

1. Igneous Rocks. *A Classification and Glossary of Terms. Recommendations of the International Union of Geological Sciences Subcommission on the Systematics of Igneous Rocks*; Le Maitre, R.W., Ed.; Cambridge University Press: New York, NY, USA, 2002; ISBN 9780521662154.
2. Jaireth, S.; Hoatson, D.M.; Mieizitis, Y. Geological setting and resources of the major rare-earth-element deposits in Australia. *Ore Geol. Rev.* **2014**, *62*, 72–128. [[CrossRef](#)]
3. Lazareva, E.V.; Zhmodik, S.M.; Dobretsov, N.L.; Tolstov, A.V.; Shcherbov, B.L.; Karmanov, N.S.; Gerasimov, E.Y.; Bryanskaya, A.V. Main minerals of abnormally high-grade ores of the Tomtor deposit (Arctic Siberia). *Russ. Geol. Geophys.* **2015**, *56*, 844–873. [[CrossRef](#)]
4. Liu, Y.-L.; Ling, M.-X.; Williams, I.S.; Yang, X.-Y.; Wang, C.Y.; Sun, W. The formation of the giant Bayan Obo REE-Nb-Fe deposit, North China, Mesoproterozoic carbonatite and overprinted Paleozoic dolomitization. *Ore Geol. Rev.* **2018**, *92*, 73–83. [[CrossRef](#)]
5. Mackay, D.A.R.; Simandl, G.J. Geology, market and supply chain of niobium and tantalum—A review. *Miner. Depos.* **2014**, *49*, 1025–1047. [[CrossRef](#)]
6. Mitchell, R.H. Primary and secondary niobium mineral deposits associated with carbonatites. *Ore Geol. Rev.* **2015**, *64*, 626–641. [[CrossRef](#)]
7. Smith, M.P.; Moore, K.; Kavecsánszki, D.; Finch, A.A.; Kynicky, J.; Wall, F. From mantle to critical zone: A review of large and giant sized deposits of the rare earth elements. *Geosci. Front.* **2016**. [[CrossRef](#)]
8. Wall, F.; Zaitsev, A.N. (Eds.) *Phoscorites and Carbonatites from Mantle to Mine: The Key Example of the Kola Alkaline Province*; Mineralogical Society: London, UK, 2004.
9. Ivanyuk, G.Y.; Yakovenchuk, V.N.; Pakhomovsky, Y.A. *Kovdor*; Laplandia Minerals: Apatity, Russia, 2002; ISBN 5900395413.
10. Mikhailova, J.A.; Kalashnikov, A.O.; Sokharev, V.A.; Pakhomovsky, Y.A.; Konopleva, N.G.; Yakovenchuk, V.N.; Bazai, A.V.; Goryainov, P.M.; Ivanyuk, G.Y. 3D mineralogical mapping of the Kovdor phoscorite–carbonatite complex (Russia). *Miner. Depos.* **2016**, *51*, 131–149. [[CrossRef](#)]

11. Ivanyuk, G.Y.; Kalashnikov, A.O.; Pakhomovsky, Y.A.; Mikhailova, J.A.; Yakovenchuk, V.N.; Konopleva, N.G.; Sokharev, V.A.; Bazai, A.V.; Goryainov, P.M. Economic minerals of the Kovdor baddeleyite-apatite-magnetite deposit, Russia: Mineralogy, spatial distribution and ore processing optimization. *Ore Geol. Rev.* **2016**, *77*, 279–311. [[CrossRef](#)]
12. Ivanyuk, G.Y.; Kalashnikov, A.O.; Pakhomovsky, Y.A.; Bazai, A.V.; Goryainov, P.M.; Mikhailova, J.A.; Yakovenchuk, V.N.; Konopleva, N.G. Subsolidus Evolution of the Magnetite-Spinel-Ulvöspinel Solid Solutions in the Kovdor phoscorite-carbonatite Complex, NW Russia. *Minerals* **2017**, *7*, 215. [[CrossRef](#)]
13. Kalashnikov, A.O.; Yakovenchuk, V.N.; Pakhomovsky, Y.A.; Bazai, A.V.; Sokharev, V.A.; Konopleva, N.G.; Mikhailova, J.A.; Goryainov, P.M.; Ivanyuk, G.Y. Scandium of the Kovdor baddeleyite-apatite-magnetite deposit (Murmansk Region, Russia): Mineralogy, spatial distribution, and potential resource. *Ore Geol. Rev.* **2016**, *72*, 532–537. [[CrossRef](#)]
14. Bell, K.; Kjarsgaard, B.A.; Simonetti, A. Carbonatites—Into the Twenty-First Century. *J. Petrol.* **1998**, *39*, 1839–1845. [[CrossRef](#)]
15. Gittins, J.; Harmer, R.E.; Barker, D.S. The bimodal composition of carbonatites: Reality or misconception? *Lithos* **2005**, *85*, 129–139. [[CrossRef](#)]
16. Mitchell, R.H. Carbonatites and carbonatites and carbonatites. *Can. Mineral.* **2005**, *43*, 2049–2068. [[CrossRef](#)]
17. Woolley, A.R.; Kjarsgaard, B.A. Paragenetic types of carbonatite as indicated by the diversity and relative abundances of associated silicate rocks: Evidence from a global database. *Can. Mineral.* **2008**, *46*, 741–752. [[CrossRef](#)]
18. Woolley, A.R.; Bailey, D.K. The crucial role of lithospheric structure in the generation and release of carbonatites: Geological evidence. *Mineral. Mag.* **2012**, *76*, 259–270. [[CrossRef](#)]
19. Jones, A.P.; Genge, M.; Carmody, L. Carbonate Melts and Carbonatites. *Rev. Mineral. Geochem.* **2013**, *75*, 289–322. [[CrossRef](#)]
20. Russell, H.D.; Hiemstra, S.A.; Groeneveld, D. The mineralogy and petrology of the Carbonatite at Loolekop, Eastern Transvaal. *S. Afr. J. Geol.* **1954**, *57*, 197–208.
21. Kukharensky, A.A.; Orlova, M.P.; Bulakh, A.G.; Bagdasarov, E.A.; Rimskaya-Korsakova, O.M.; Nefedov, E.I.; Ilyinsky, G.A.; Sergeev, A.S.; Abakumova, N.B. *Caledonian Complex of Ultrabasic, Alkaline Rocks and Carbonatites of Kola Peninsula and Northern Karelia (Geology, Petrology, Mineralogy and Geochemistry) (in Russian)*; Nedra: Moscow, Russia, 1965.
22. Yegorov, L.S. Phoscorites of the Maymecha-Kotuy ijolite-carbonatite association. *Int. Geol. Rev.* **1993**, *35*, 346–358. [[CrossRef](#)]
23. Rimskaya-Korsakova, O.M. On Question about Genesis of the Kovdor Iron-Ore Deposit. In *Problems of Magmatism and Metamorphism (in Russian)*; Leningrad State University Publishing: Leningrad, Russia, 1963; pp. 125–142.
24. Kalashnikov, A.O.; Ivanyuk, G.Y.; Mikhailova, J.A.; Sokharev, V.A. Approach of automatic 3D geological mapping: The case of the Kovdor phoscorite-carbonatite complex, NW Russia. *Sci. Rep.* **2017**, *7*, 1–13. [[CrossRef](#)] [[PubMed](#)]
25. Ternovoy, V.I. *Carbonatite Massifs and Their Mineral Resources (in Russian)*; Leningrad State University: Leningrad, Russia, 1977.
26. Afanasyev, B. *Mineral Resources of Alkaline-Ultrabasic Massifs of the Kola Peninsula (in Russian)*; Roza Vetrov Publishing: Saint-Petersburg, Russia, 2011.
27. Dunaev, V.A. Structure of the Kovdor deposit (in Russian). *Geol. Ore Depos.* **1982**, *3*, 28–36.
28. Kapustin, Y.L. *Mineralogy of Carbonatites*; Amerind Publishing: New Delhi, India, 1980.
29. Krasnova, N.I.; Kopylova, L.N. The Geologic Basis for Mineral-Technological Mapping at the Kovdor Ore Deposit. *Int. Geol. Rev.* **1988**, *30*, 307–319. [[CrossRef](#)]
30. Krasnova, N.I.; Petrov, T.G.; Balaganskaya, E.G.; García, D.; Moutte, J.; Zaitsev, A.N.; Wall, F. Introduction to phoscorites: Occurrence, composition, nomenclature and petrogenesis. In *Phoscorites and Carbonatites from Mantle to Mine: The Key Example of the Kola Alkaline Province*; Zaitsev, A.N., Wall, F., Eds.; Mineralogical Society: London, UK, 2004; pp. 43–72. ISBN 0-903056-22-4.
31. Bayanova, T.B.; Kirnarsky, Y.M.; Levkovich, N.V. U-Pb dating of baddeleyite from Kovdor massif (in Russian). *Dokl. Earth Sci.* **1997**, *356*, 509–511.
32. Amelin, Y.; Zaitsev, A.N. Precise geochronology of phoscorites and carbonatites: The critical role of U-series disequilibrium in age interpretations. *Geochim. Cosmochim. Acta* **2002**, *66*, 2399–2419. [[CrossRef](#)]

33. Rodionov, N.V.; Belyatsky, B.V.; Antonov, A.V.; Kapitonov, I.N.; Sergeev, S.A. Comparative in-situ U–Th–Pb geochronology and trace element composition of baddeleyite and low-U zircon from carbonatites of the Palaeozoic Kovdor alkaline–ultramafic complex, Kola Peninsula, Russia. *Gondwana Res.* **2012**, *21*, 728–744. [CrossRef]
34. Rimskaya-Korsakova, O.M.; Krasnova, N.I. *Geology of Deposits of the Kovdor Massif (in Russian)*; St. Petersburg University Press: Saint Petersburg, Russia, 2002.
35. Shats, L.; Sorokina, I.; Kalinkin, M.; Korniyushin, A. *Report on Geophysical Works Made by the Kovdor Geological Party in the Area of Kovdor in 1966 (in Russian)*; Archives of the Natural Reserves Department of the Murmansk region: Apatity, Russia, 1967.
36. ImageJ, Open Source Image Processing Software. Available online: <http://imagej.net/> (accessed on 19 June 2018).
37. Sheldrick, G.M. A short history of SHELX. *Acta Crystallogr. Sect. A Found. Crystallogr.* **2008**, *64*, 112–122. [CrossRef] [PubMed]
38. Dolomanov, O.V.; Bourhis, L.J.; Gildea, R.J.; Howard, J.A.K.; Puschmann, H. OLEX2: A complete structure solution, refinement and analysis program. *J. Appl. Crystallogr.* **2009**, *42*, 339–341. [CrossRef]
39. Agilent CrysAlis PRO. 2014. Available online: <https://www.rigaku.com/en/products/smc/crystalis> (accessed on 19 June 2018).
40. Momma, K.; Izumi, F. VESTA 3 for three-dimensional visualization of crystal, volumetric and morphology data. *J. Appl. Crystallogr.* **2011**, *44*, 1272–1276. [CrossRef]
41. Putz, H.; Brandenburg, K. *Diamond–Crystal and Molecular Structure Visualization*; Crystal Impact GbR: Bonn, Germany, 2012.
42. Dolivo-Dobrovolsky, D.D. MINAL, Free Software. Available online: <http://www.dimadd.ru> (accessed on 8 July 2013).
43. StatSoft Inc, Statistica 8. Available online: www.statsoft.ru (accessed on 19 June 2018).
44. TableCurve 2D. Available online: www.sigmaplot.co.uk/products/tablecurve2d/tablecurve2d.php (accessed on 19 June 2018).
45. Micromine Pty Ltd. Micromine 16.1. Available online: <https://www.micromine.com/> (accessed on 19 June 2018).
46. Veksler, I.V.; Nielsen, T.F.D.; Sokolov, S.V. Mineralogy of Crystallized Melt Inclusions from Gardiner and Kovdor Ultramafic Alkaline Complexes: Implications for Carbonatite Genesis. *J. Petrol.* **1998**, *39*, 2015–2031. [CrossRef]
47. Tarasenko, Y.; Litsarev, M.A.; Tretyakova, L.I.; Vokhmentsev, A.Y. Chrysolite of the Kovdor phlogopite deposit (in Russian). *Izv. AN SSSR Seriya Geol.* **1986**, *9*, 67–80.
48. Zeira, S.; Hafner, S.S. The location of Fe³⁺ ions in forsterite (Mg₂SiO₄). *Earth Planet. Sci. Lett.* **1974**, *21*, 201–208. [CrossRef]
49. Janney, D.E.; Banfield, J.F. Distribution of cations and vacancies and the structure of defects in oxidized intermediate olivine by atomic-resolution TEM and image simulation. *Am. Mineral.* **1998**, *83*, 799–810. [CrossRef]
50. Bragg, W.L.; Brown, G.B. XXX. Die Struktur des Olivins. *Z. Krist. Cryst. Mater.* **1926**, *63*, 538–556. [CrossRef]
51. Brown, G.E. *Crystal Chemistry of the Olivines*; Virginia Polytechnic Institute and State University: Blacksburg, VA, USA, 1970.
52. Huggins, F.E. Cation order in olivines: Evidence from vibrational spectra. *Chem. Geol.* **1973**, *11*, 99–108. [CrossRef]
53. Nover, G.; Will, G. Structure refinements of seven natural olivine crystals and the influence of the oxygen partial pressure on the cation distribution. *Z. Krist. Cryst. Mater.* **1981**, *155*. [CrossRef]
54. Francis, C.A. New data on the forsterite-tephroite series. *Am. Mineral.* **1985**, *70*, 568–575.
55. Seifert, F.A.; Virgo, D. Kinetics of the Fe²⁺-Mg, Order-Disorder Reaction in Anthophyllites: Quantitative Cooling Rates. *Science* **1975**, *188*, 1107–1109. [CrossRef] [PubMed]
56. Seifert, F.; Virgo, D. Temperature dependence of intracrystalline Fe²⁺-Mg distribution in a natural anthophyllite. In *Carnegie Institute of Washington Year Book*; Carnegie Institute of Washington: Washington, DC, USA, 1974; pp. 405–411.
57. Shannon, R.D. Revised effective ionic radii and systematic studies of interatomic distances in halides and chalcogenides. *Acta Crystallogr. Sect. A* **1976**, *32*, 751–767. [CrossRef]

58. Riekel, C.; Weiss, A. Cation-Ordering in Synthetic $\text{Mg}_{2-x}\text{Fe}_x\text{SiO}_4$ -Olivines. *Z. Naturforsch. B* **1978**, *33*. [[CrossRef](#)]
59. Redfern, S.A.T.; Henderson, C.M.B.; Knight, K.S.; Wood, B.J. High-temperature order-disorder in $(\text{Fe}_{0.5}\text{Mn}_{0.5})_2\text{SiO}_4$ and $(\text{Mg}_{0.5}\text{Mn}_{0.5})_2\text{SiO}_4$ olivines: An in situ neutron diffraction study. *Eur. J. Mineral.* **1997**, *9*, 287–300. [[CrossRef](#)]
60. Shen, B.; Tamada, O.; Kitamura, M.; Morimoto, N. Superstructure of laihunite-3M ($\square_{0.40}\text{Fe}^{2+}_{0.80}\text{Fe}^{3+}_{0.80}\text{SiO}_4$). *Am. Mineral.* **1986**, *71*, 1455–1460.
61. Brown, G.E.; Prewitt, C.T. High-temperature crystal chemistry of hortonolite. *Am. Mineral.* **1973**, *58*, 577–587.
62. Princivalle, F.; Secco, L. Crystal structure refinement of 13 olivines in the forsterite-fayalite series from volcanic rocks and ultramafic nodules. *TMPM* **1985**, *34*, 105–115. [[CrossRef](#)]
63. Motoyama, T.; Matsumoto, T. The crystal structures and the cation distributions of Mg and Fe of natural olivines. *Miner. J.* **1989**, *14*, 338–350. [[CrossRef](#)]
64. Princivalle, F. Influence of temperature and composition on Mg-Fe²⁺ intracrystalline distribution in olivines. *Mineral. Petrol.* **1990**, *43*, 121–129. [[CrossRef](#)]
65. Heinemann, R.; Kroll, H.; Kirfel, A.; Barbier, B. Order and anti-order in olivine III: Variation of the cation distribution in the Fe,Mg olivine solid solution series with temperature and composition. *Eur. J. Mineral.* **2007**, *19*, 15–27. [[CrossRef](#)]
66. Kroll, H.; Kirfel, A.; Heinemann, R.; Barbier, B. Volume thermal expansion and related thermophysical parameters in the Mg, Fe olivine solid-solution series. *Eur. J. Mineral.* **2012**, *24*, 935–956. [[CrossRef](#)]
67. Ren, Y.; Chen, F.; Yang, J.; Gao, Y. Exsolution of Diopside and Magnetite in Olivine from Mantle Dunite, Luobusa Ophiolite, Tibet, China. *Acta Geol. Sin. Engl. Ed.* **2010**, *82*, 377–384. [[CrossRef](#)]
68. Markl, G.; Marks, M.A.W.; Wirth, R. The influence of T, aSiO₂, and fO₂ on exsolution textures in Fe-Mg olivine: An example from augite syenites of the Ilimaussaq Intrusion, South Greenland. *Am. Mineral.* **2001**, *86*, 36–46. [[CrossRef](#)]
69. Libourel, G. Systematics of calcium partitioning between olivine and silicate melt: Implications for melt structure and calcium content of magmatic olivines. *Contrib. Mineral. Petrol.* **1999**, *136*, 63–80. [[CrossRef](#)]
70. Carmichael, I.S.E.; Nicholls, J. Iron-titanium oxides and oxygen fugacities in volcanic rocks. *J. Geophys. Res.* **1967**, *72*, 4665–4687. [[CrossRef](#)]
71. Mysen, B.O.; Richet, P. *Silicate Glasses and Melts. Properties and Structure*; Elsevier: New York, NY, USA, 2005; ISBN 0-444-52011-2.
72. Moseley, D. Symplectic exsolution in olivine. *Am. Mineral.* **1984**, *69*, 139–153.
73. Wyllie, P.J.; Baker, M.B.; White, B.S. Experimental boundaries for the origin and evolution of carbonatites. *Lithos* **1990**, *26*, 3–19. [[CrossRef](#)]
74. Veksler, I.V.; Petibon, C.; Jenner, G.A.; Dorfman, A.M.; Dingwell, D.B. Trace Element Partitioning in Immiscible Silicate-Carbonate Liquid Systems: An Initial Experimental Study Using a Centrifuge Autoclave. *J. Petrol.* **1998**, *39*, 2095–2104. [[CrossRef](#)]
75. Wyllie, P.J.; Tuttle, O.F. The System CaO-CO₂-H₂O and the Origin of Carbonatites. *J. Petrol.* **1960**, *1*, 1–46. [[CrossRef](#)]
76. Koster van Groos, A.F.; Wyllie, P.J. Liquid immiscibility in the system Na₂O-Al₂O₃-SiO₂-CO₂ at pressures to 1 kilobar. *Am. J. Sci.* **1966**, *264*, 234–255. [[CrossRef](#)]
77. Koster van Groos, A.F.; Wyllie, P.J. Liquid immiscibility in the join NaAlSi₃O₈-Na₂CO₃-H₂O and its bearing on the genesis of carbonatites. *Am. J. Sci.* **1968**, *266*, 932–967. [[CrossRef](#)]
78. Freestone, I.C.; Hamilton, D.L. The role of liquid immiscibility in the genesis of carbonatites? An experimental study. *Contrib. Mineral. Petrol.* **1980**, *73*, 105–117. [[CrossRef](#)]
79. Kjarsgaard, B.A.; Hamilton, D.L. Liquid immiscibility and the origin of alkali-poor carbonatites. *Mineral. Mag.* **1988**, *52*, 43–55. [[CrossRef](#)]
80. Kjarsgaard, B.A.; Hamilton, D.L. The genesis of carbonatites by liquid immiscibility. In *Carbonatites: Genesis and Evolution*; Bell, K.E., Ed.; Unwin Hyman: London, UK, 1989; pp. 388–404.
81. Watkinson, D.H.; Wyllie, P.J. Experimental Study of the Composition Join NaAlSiO₄-CaCO₃-H₂O and the Genesis of Alkaline Rock—Carbonatite Complexes. *J. Petrol.* **1971**, *12*, 357–378. [[CrossRef](#)]
82. Franz, G.W. *Melting Relationships in the System CaO-MgO-SiO₂-CO₂-H₂O: A Study of Synthetic Kimberlites*; The Pennsylvania State University: State College, PA, USA, 1965.

83. Franz, G.W.; Wyllie, P.J. Experimental Studies in the system CaO-MgO-SiO₂-CO₂-H₂O. In *Ultramafic and Related Rocks*; Wyllie, P.J., Ed.; John Wiley and Sons: New York, NY, USA, 1967; pp. 323–326.
84. Toplis, M.J.; Libourel, G.; Carroll, M.R. The role of phosphorus in crystallisation processes of basalt: An experimental study. *Geochim. Cosmochim. Acta* **1994**, *58*, 797–810. [[CrossRef](#)]
85. Mysen, B.O. Iron and phosphorus in calcium silicate quenched melts. *Chem. Geol.* **1992**, *98*, 175–202. [[CrossRef](#)]
86. Mysen, B.O.; Ryerson, F.J.; Virgo, D. The structural role of phosphorus in silicate melts. *Am. Mineral.* **1981**, *66*, 106–117.
87. Mikhailova, J.A.; Krasnova, N.I.; Krezer, Y.L.; Wall, F. Inclusions in minerals of the Kovdor intrusion of ultrabasic, alkaline rocks and carbonatites as indicators of the endogenic evolution processes. In *Deep-Seated Magmatism, Magmatic Sources and the Problem of Plumes (in Russian)*; Vladykin, N.V., Ed.; Siberian Branch of the Russian Academy of Sciences: Irkutsk/Valdivostok, Russia, 2002; pp. 296–320.
88. Biggar, G.M. *High Pressure High Temperature Phase Equilibrium Studies in the System CaO-CaF₂-P₂O₅-H₂O-CO₂ with Special Reference to the Apatites*; University of Leeds: Leeds, UK, 1962.
89. Wyllie, P.J.; Biggar, G.M. Fractional Crystallization in the “Carbonatite Systems” CaO-MgO-CO₂-H₂O and CaO-CaF₂-P₂O₅-CO₂-H₂O. In *Papers and Proceedings of the Fourth General Meeting. International Mineralogical Association*; International Mineralogical Association: Gauteng, South Africa, 1966; pp. 92–105.
90. Wyllie, P.; Haas, J. The system CaO-SiO₂-CO₂-H₂O: 1. Melting relationships with excess vapor at 1 kilobar pressure. *Geochim. Cosmochim. Acta* **1965**, *29*, 871–892. [[CrossRef](#)]
91. Moussallam, Y.; Florian, P.; Corradini, D.; Morizet, Y.; Sator, N.; Vuilleumier, R.; Guillot, B.; Iacono-Marziano, G.; Schmidt, B.C.; Gaillard, F. The molecular structure of melts along the carbonatite-kimberlite-basalt compositional joint: CO₂ and polymerisation. *Earth Planet. Sci. Lett.* **2016**, *434*, 129–140. [[CrossRef](#)]
92. Klemme, S. Experimental constraints on the evolution of iron and phosphorus-rich melts: Experiments in the system CaO-MgO-Fe₂O₃-P₂O₅-SiO₂-H₂O-CO₂. *J. Mineral. Petrol. Sci.* **2010**, *105*, 1–8. [[CrossRef](#)]
93. Eberl, D.D.; Kile, D.E.; Drits, V.A. On geological interpretations of crystal size distributions: Constant vs. proportionate growth. *Am. Mineral.* **2002**, *87*, 1235–1241. [[CrossRef](#)]
94. Minarik, W.G.; Watson, E.B. Interconnectivity of carbonate melt at low melt fraction. *Earth Planet. Sci. Lett.* **1995**, *133*, 423–437. [[CrossRef](#)]
95. Minarik, W.G. Complications to Carbonate Melt Mobility due to the Presence of an Immiscible Silicate Melt. *J. Petrol.* **1998**, *39*, 1965–1973. [[CrossRef](#)]
96. Keppler, H. Water solubility in carbonatite melts. *Am. Mineral.* **2003**, *88*, 1822–1824. [[CrossRef](#)]
97. Krasnova, N.I. Geology, mineralogy and problems of genesis of apatite-francolite rocks of the Kovdor massif (in Russian). In *Composition of Phosphorites*; Nauka: Novosibirsk, Russia, 1979; pp. 164–172.

